Advances in Water Resources 209 (2026) 105223

Contents lists available at ScienceDirect

Advances in Water Resources

journal homepage: www.elsevier.com/locate/advwatres

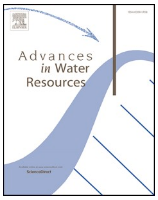

# Increasing the fidelity of hyperlocal simulations of urban pluvial flooding through street flooding observations

S. Annis [a], M.G. Badas [a], G. Mascaro [b,*]

[a] Dipartimento di Ingegneria Civile, Ambientale ed Architettura, Università di Cagliari, Italy
[b] School of Sustainable Engineering and the Built Environment, Arizona State University, USA

## ARTICLE INFO

*Keywords:*
Pluvial flooding
Urban basin
Urban hydrology
Flood monitoring
Hydrodynamic models
New York City
Sewer modeling

## ABSTRACT

Urban pluvial flooding is a highly impactful natural hazard whose understanding remains limited by the scarcity of observations. Here, we demonstrated that continuous, spatially distributed, street-level flood depth measurements provide critical information to increase the fidelity of pluvial flooding simulations. We applied the LISFLOOD-FP two-dimensional, rain-on-grid hydrodynamic model to two dense urban basins of 10.9 and 0.8 km$^2$, respectively, in New York City (NYC), where eight sensors from the FloodNet network recorded widespread flooding during three intense storms. We first provided insights into the generation of model domain and net precipitation forcings at the hyperlocal resolution of 1 m, required to quantify flood hazards at the pedestrian and vehicle scale and to support decision-making. We then focused on one event in the larger basin and assessed the performance of three modeling scenarios under the common condition of limited information about the underground sewer network. We found that neglecting the sewer or simplifying its effect by reducing the precipitation rates severely overestimated the observed water depths. In contrast, simulations based on runoff removal at the stormwater inlets reproduced the observed hydrographs remarkably well after calibration of a single coefficient in the outflow relationship against the sensor data. This calibrated approach proved robust, maintaining high performance in the smaller basin across all three events. As street-level flood observations become increasingly available, the proposed methods could help identify the most accurate strategies to model pluvial flooding in diverse urban landscapes under varying levels of data availability.

## 1. Introduction

Floods are the most frequent natural disasters, causing significant socioeconomic, health, and environmental impacts (CRED and UNDRR, 2020; NCEI, 2025). Flood impacts are high in urban regions because (1) the greater fraction of impervious surfaces leads to larger runoff coefficients and the lower terrain roughness favors high flow velocities and reduces the time-to-peak (Feng et al., 2021; Hollis, 1975; Jacobson, 2011), and (2) cities have high vulnerability and exposure due to the concentration of people, economic activities, and real estate and infrastructure assets (National Academies of Sciences, Engineering, and Medicine, 2019).

The main drivers of urban flooding are fluvial, which occurs when water flowing in a river overtops the levees; coastal, which is due to ocean tides and storm surges; and pluvial, which results from intense precipitation that exceeds the drainage capacity of the natural landscape (e.g., interception, infiltration) and stormwater infrastructure (Rosenzweig et al., 2018). Compared to the first two mechanisms, pluvial flooding has been considered a relatively minor hazard for a long time because it was assumed that the stormwater infrastructure was properly designed to minimize its occurrence and impacts. For example, the U.S. Federal Emergency Management Service (FEMA) does not include pluvial flooding in its national directives (FEMA, 2023a). However, the stormwater infrastructure has been modified over time according to different design standards (Underwood et al., 2020), and its layout and properties are often unknown. Therefore, every time the urban landscapes are altered and parts of the stormwater sewer are retrofitted, the performance of the entire sewer network cannot be accurately assessed, resulting in a possibly higher flooding hazard than what was assumed during design.

The reviews by Hammond et al. (2013) and Agonafir et al. (2023) reported several studies highlighting that pluvial flooding in urban regions causes direct tangible impacts by damaging buildings, infrastructure, and vehicles; indirect tangible consequences by interrupting

---

* Corresponding author: Hydrosystems Engineering, WCPH, Room 416, 777 E. University Dr., Tempe, AZ USA.
*E-mail address:* gmascaro@asu.edu (G. Mascaro).

https://doi.org/10.1016/j.advwatres.2026.105223
Received 8 November 2025; Received in revised form 26 January 2026; Accepted 26 January 2026
Available online 27 January 2026
0309-1708/© 2026 The Authors. Published by Elsevier Ltd. This is an open access article under the CC BY-NC-ND license (http://creativecommons.org/licenses/by-nc-nd/4.0/).

businesses and infrastructure services; and intangible damages on health (casualties, injures, mental health effects, floodwater pollution) and the environment, which can manifest close to and sometime after the event. Recent efforts have also emphasized the negative impacts of more frequent and less severe flood events, known as nuisance flooding (Moftakhari et al., 2018).

Despite pluvial flooding being increasingly recognized as a critical issue in urban stormwater management (Rosenzweig et al., 2018), the knowledge of and the ability to accurately simulate this natural hazard are still limited largely because of the lack of continuous observations of street-level flood water variables at distributed locations (Drews et al., 2023). Current simulation approaches relying on hydrologic and hydrodynamic models with varying levels of complexities have only been validated with alternative datasets including: water depth measurements in laboratory physical models (e.g., Fraga et al., 2017; Mignot et al., 2019; Sañudo et al., 2025); outputs of numerical models that explicitly account for most physical processes and incorporate stormwater infrastructure, which are treated as “observations” (e.g., Montalvo et al., 2024; Oberauer and Lehmann, 2024; Xiang et al., 2024); sparse estimates of flood water depth from pictures published on social media platforms and news outlets (Drews et al., 2023; Guan et al., 2023; Guo et al., 2023); and proxies of flooding hotspots like insurance claims (Gradeci et al., 2019). While these validation strategies have demonstrated value in improving flood models, they do not allow the quantitative assessment of their ability to capture the spatiotemporal dynamics of observed pluvial flood events in real-world urban catchments.

In this study, we addressed this critical need, to our knowledge for the first time, using spatially distributed, continuous street-level water depth (*h*) data from the FloodNet network in New York City (NYC). FloodNet is a partnership between academic researchers and public agencies started in 2021, which has developed and installed ultrasonic sensors that continuously record the presence, depth, and duration of street-level floods in the five NYC boroughs (Mydlarz et al., 2024). Currently, over 200 sensors have been deployed, and more are planned to be installed.

Using these unique observations, we provided the first quantitative evaluation of commonly used pluvial flood modeling approaches based on direct, time-varying measurements of street-level *h*, thereby addressing the limitations of spatial-only or event-integrated validations approaches that are typically adopted. Specifically, we assessed three modeling approaches that are widely applied to simulate pluvial flooding with limited information on the stormwater sewer network (hereafter referred to as the sewer, for brevity), which is typical in most cities (see Section 4.1 for a brief literature review on flood modeling approaches). The methods rely on simulations with a rain-on-grid two-dimensional (2D) hydrodynamic model where (1) the sewer is not considered, (2) the precipitation rate used to design the sewer is removed from the net precipitation input grids, and (3) distributed sinks are introduced at the stormwater inlet locations using a single outflow relationship.

Here, we adopted the open-source LISFPLOOD-FP as the 2D rain-on-grid hydrodynamic model (Bates and De Roo, 2000; Sharifian et al., 2023) and applied it at the hyperlocal (meter-scale) resolution of 1 m, which is needed to quantify flood hazards for pedestrians, vehicles, and buildings (FEMA, 2025). We initially provided methodological and practical insights for setting up and applying 2D hydrodynamic models in complex urban environments at hyperlocal scales. These include procedures to generate model domains that explicitly represent key urban landscape features affecting flow dynamics, such as buildings, streets, and local depressions; and to create net precipitation grids that account for building roofs and losses due to vegetation interception and infiltration in pervious areas. While these elements are often treated implicitly or in isolation in prior studies, here they were integrated into a coherent, observation-tested workflow.

We used these insights to apply LISFPLOOD-FP in two urban catchments in the borough of Brooklyn using high-resolution geospatial data from the NYC OpenData public repository (City of New York, 2025). The catchments have areas of 10.9 km$^2$ and 0.8 km$^2$ and include six and two FloodNet sensors, respectively; they have similar building density and imperviousness but marked differences in steepness. No information on the sewer is available apart from the stormwater inlet locations. We then evaluated the three modeling strategies in the larger catchment for an intense event caused by Tropical Storm Ophelia in 2023 by comparing distributed model outputs with the sensors’ measurements. Subsequently, we verified the robustness of the best-performing method, calibrated in the large basin, by applying it to a smaller and steeper catchment to simulate the same event and two additional floods generated by Tropical Storm Henri and Hurricane Ida in 2021. Finally, we showed that these hyperlocal simulations reproduce flood dynamics with high fidelity and enable the identification of basin areas experiencing varying levels of flood hazard, with the spatial and temporal resolution required for decision-making.

This study demonstrates the value of street-level flood observations for quantifying the accuracy of pluvial flood models and guiding the selection of the most appropriate simulation approach under data constraints. The proposed framework advances current understanding of urban pluvial flood modeling and facilitates the application of hyperlocal simulations to support effective flood risk management and adaptation planning.

## 2. Study area and datasets

Our study sites are two urban watersheds of 10.9 km$^2$ and 0.8 km$^2$ in the borough of Brooklyn, New York City (NYC; Fig. 1a), selected because (1) they include six and two FloodNet sensors, respectively (Figs. 1b-d), that detected pluvial flooding during the analyzed storms (described in Section 3); (2) they are close to a high-resolution rain gauge of the New York State Mesonet network (Brotzge et al., 2020; Figs. 1a,b); and (3) they have markedly different terrain properties, which makes them valuable case studies to assess model robustness. We tested all modeling approaches in the larger basin (hereafter, the calibration basin or CB) and evaluated the transferability of the best-performing method in the smaller catchment (hereafter, the validation basin or VB). The latter is in a historically flood-prone region where the first FloodNet sensors were placed, providing longer water depth records. To set up the model in the basins, we used several geospatial datasets from the NYC OpenData portal, listed in Table 1, along with key details, sources, and how they were utilized in this study. The datasets cover the entire city and were reprojected in UTM zone 18 N (EPSG code 26,918). The grids were aggregated at 1-m resolution; the same was done with the vector data after they were rasterized.

We delineated the basin boundaries from the Topobathy LiDAR Hydroenforced digital elevation model (DEM), which provides the surface elevation without vegetation and anthropogenic features (e.g., buildings) and includes hydroenforcement breaklines that allow water to flow through artificial pathways (e.g., culverts) that are not represented in the DEM (OCM Partners, 2017). The DEM was processed with Geographic Resources Analysis Support System (GRASS) libraries within the QGIS software (QGIS Development Team, 2019) to create the flow direction and accumulation grids and, subsequently, the stream network using a threshold value of 200,000 m$^2$. We performed the latter task with the GRASS *r.watershed* module, which uses the least cost path algorithm to route flow out of depressions without applying any fill depression algorithm (Metz et al., 2011). We retained these depressions to accurately represent localized flooding. To support this choice, we thoroughly inspected the depressions in the DEM and found that the vast majority correspond to realistic features (e.g., low-lying parking areas, railroads, and basements), with only a small number likely attributable due to DEM errors (see Section 6.3 and Figures S2-S10).

The basins’ DEMs are displayed in Fig. 2, along with a zoom on the area close to the outlet where the FloodNet sensors are installed and a three-dimensional view of such area. As expected for urban basins, the

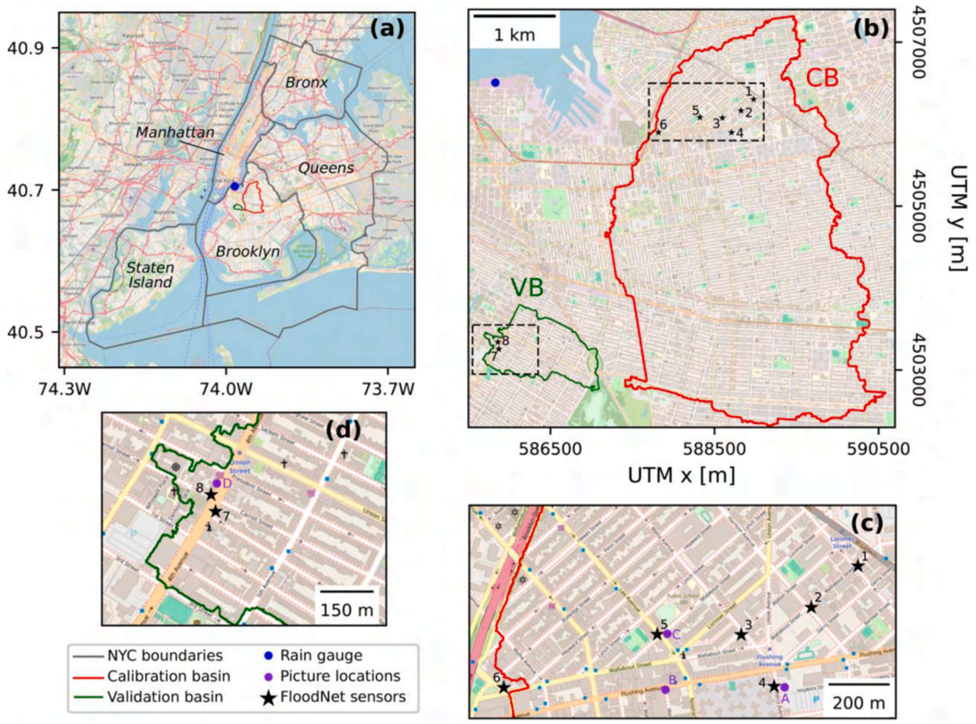

**Fig. 1.** (a) Study basins in NYC in the borough of Brooklyn, along with the other four boroughs and the rain gauge of the New York State Mesonet network (latitude = 40.705°, longitude = −73.984°). (b) Basins' boundaries with the FloodNet sensors (numbered from 1 to 8; see Table S1) reported in UTM zone 18 N (EPSG code 26,918); CB = calibration basin, VB = validation basin. (c)-(d) Zoom on the regions of the FloodNet sensors (dashed rectangles in panel (b)) in the two basins; panels (c)-(d) also show the sites A, B, C, and D of the pictures reported in Fig. 4. The base maps displayed in the panels are from OpenStreetMap.

**Table 1**
Geospatial datasets obtained from the NYC OpenData portal used for the basin identification and the hydrologic-hydraulic simulations.

| Dataset Name | Variable | Resolution | Year | Reference | Use |
|---|---|---|---|---|---|
| Topobathy LiDAR Hydroenforced Digital Terrain Model | Elevation with all vegetation and anthropogenic features removed | 1 foot (0.3 m) | 2017 | OCM Partners (2017) | Basin delineation, terrain file for LISFLOOD-FP |
| Land Cover Raster Data | Eight land cover classes | 6 inches (0.15 m) | 2017 | OTI (2017) | Definition of (1) impervious areas and saturated hydraulic conductivity in the generation of effective precipitation, and (2) Manning's roughness in LISFLOOD-FP |
| Building Footprints | Polygons with building footprints | NA | 2016 | OTI (2016) | Terrain file for LISFLOOD-FP |
| Stormwater Inlets | Points with location of stormwater inlets | Point | 2017 | DEP (2017) | Incorporation of stormwater infrastructure in the simulations |
| Tree Location | Points with tree location | Point | 2015 | DPR (2017) | Identification of tree pits for the calculation of water infiltration into the soil |

stream networks do not consist of actual channels but correspond to the road network paths with the highest flow accumulation values. In the CB (Fig. 2a-c), elevation declines steadily by ~60 m over ~4 km extending from the southern part to the outlet area, where the terrain is relatively flat. The VB (Fig. 2d-f) is much steeper, with elevation changing by ~50 m in only ~1.2 km. The three-dimensional views demonstrate that the high resolution of the LiDAR-based DEM captures small-scale elevation changes affecting local water flow.

As reported in Table 2 and shown in Fig. 3, the basins are densely urbanized and largely impervious. Buildings, roads, and other impervious surfaces cover 75.3% (70.4%) of the CB (VB) area. Vegetation accounts for most of the remaining area, with trees covering 21.1% (27.0%) of the basin and being mostly placed in pits along streets, and grass/shrubs areas accounting for 3.0% (2.6%). Other land cover classes represent a negligible fraction of the basin area. To complete the basins' characterization and the model setup, we also acquired the building footprint and the stormwater inlets' location datasets from the city (Table 1).

We obtained precipitation data at 5-minute resolution from a rain gauge of the New York State Mesonet network located on Gold Street, Brooklyn, just 2.1 and 3.0 km from the CB and VB outlets, respectively (Fig. 1b). We acquired water depth data from eight FloodNet sensors (Fig. 1b-d) at 1-minute resolution, with some gaps caused by issues in the data transmission network (Mydlarz, personal communication). Table S1 in the Supporting Information reports the sensors' location and the drainage area that ranges from 0.2 to 10.9 km$^2$ (0.15 to 0.79 km$^2$) in the CB (VB).

## 3. The simulated pluvial flood events

We focused on three heavy precipitation events that caused widespread flooding in the basins. Two events occurred in 2021 as remnants of Tropical Storm Henri on August 21 (Pasch et al., 2022) and Hurricane Ida on September 1 (FEMA, 2023b), respectively. The third event happened on September 29, 2023, as a remnant of Tropical Storm Ophelia (WPC, 2023). Because of the time of FloodNet sensors'

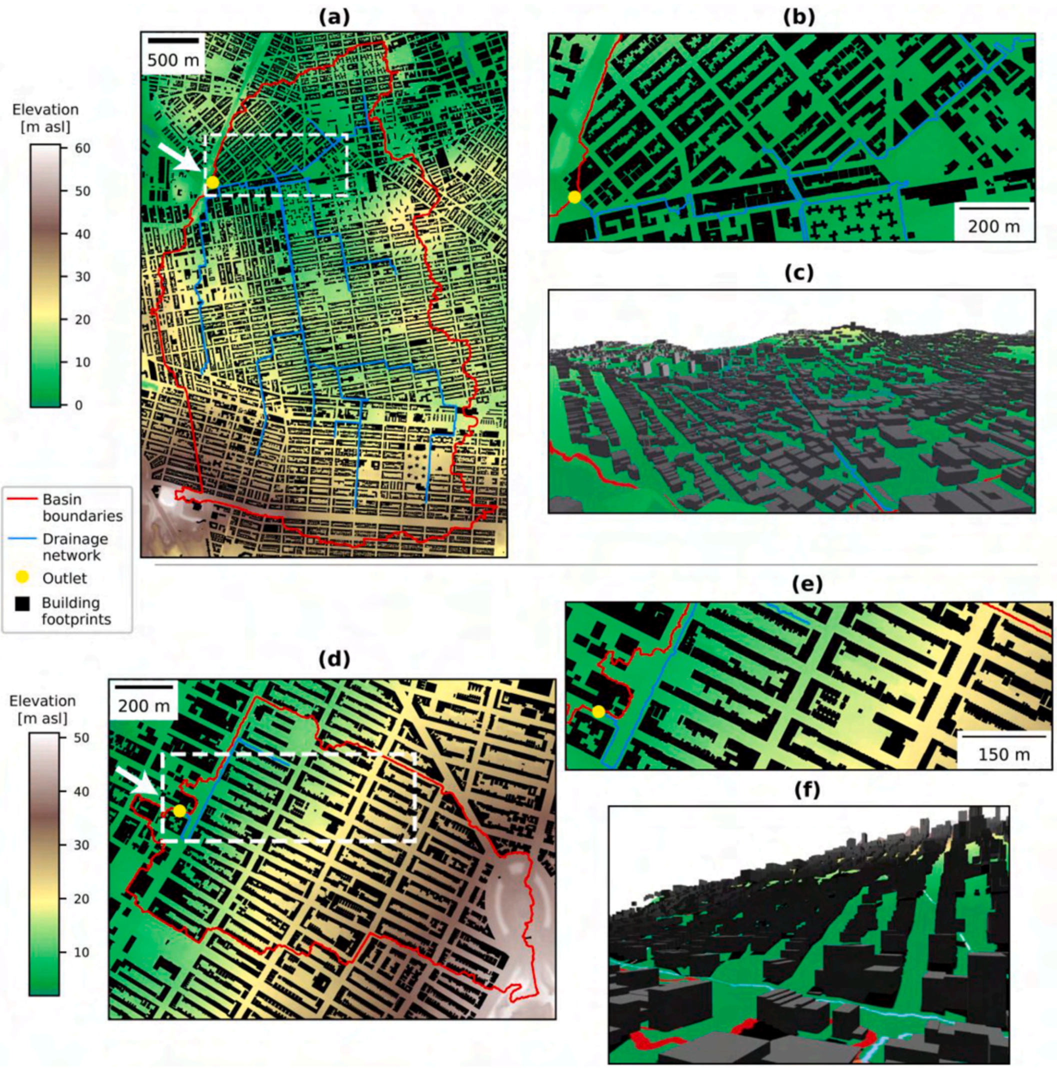

**Fig. 2.** (a) DEM of the calibration basin (CB) with the building footprints, surface drainage network (i.e., roadways with the highest flow accumulation values), and outlet. (b) Zoom on the outlet region and the sensors (white rectangle in panel (a)). (c) Three-dimensional view of the area shown in (b) from an observer located just west of the outlet, with the viewpoint indicated by the arrow in panel (a). (d)-(f) Same as (a)-(c) but for the validation basin (VB).

**Table 2**
Land cover classes with their percentage in the calibration and validation basins and corresponding Manning's roughness derived from Van Der Sande et al. (2003).

| Land cover class | Percent area in the calibration basin | Percent area in the validation basin | Manning's roughness, $n$ |
|---|---|---|---|
| | **(%)** | **(%)** | **(s m$^{1/3}$)** |
| Tree canopy | 21.1 | 27.0 | 0.05 |
| Grass/shrubs | 3.0 | 2.6 | 0.1 |
| Bare soils | 0.1 | 0.0 | 0.02 |
| Water | 0.0 | 0.0 | 0.03 |
| Buildings | 33.5 | 37.9 | 0.2 |
| Roads | 13.6 | 11.6 | 0.013 |
| Railroads | 0.5 | 0.0 | 0.033 |
| Other impervious | 28.2 | 20.9 | 0.05 |

installation, flooding caused by Henri and Ida was only observed in the VB at one sensor, while all eight sensors measured street flooding caused by Ophelia in the two basins. The three events caused significant impacts in NYC, although with different severity, including disruptions in the transportation systems, road closures, power outages, roof collapses, and flooded basements. Ida resulted in 13 fatalities attributed to flooding.

The precipitation hyetographs recorded by the gage close to the study basins are reported in Figs. 4a-c. Two main storms caused by Henri occurred over ~5 h (labeled as St1 and St2 in Fig. 4a), a single storm concentrated in ~8 h during Ida (St1 in Fig. 4b), and three main storms over ~10.5 h (St1-St3 in Fig. 4c) within Ophelia. According to the intensity-duration-frequency curves at La Guardia Airport from NOAA Atlas 14 (Fig. 4d; Perica et al., 2015), the return periods of the maximum observed precipitation depths exceeded 10 years for durations above 1 h for all events and 100 years for some durations during Ida and Ophelia. Since the sewer has been largely designed for the 5-year return period, significant flooding conditions were observed in the study basins (Fig. 4d). This led to nonzero water depth recorded at the eight FloodNet sensors with peaks between 0.3 and almost 1 m (see Section 5.1).

## 4. Hydrologic-hydraulic modeling framework, setup, and simulations

### 4.1. Brief overview of current pluvial flood modeling approaches

Before describing the modeling approaches tested in this study, we briefly review the methods currently available for simulating pluvial flooding in urban areas. The most accurate simulations require the

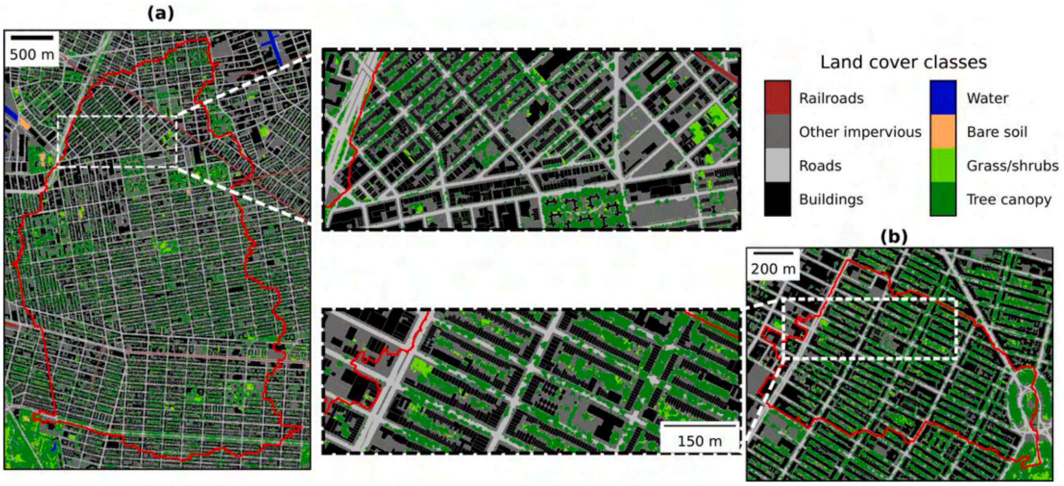

**Fig. 3.** Land cover maps of the (a) calibration (CB) and (b) validation (VB) basins, along with a zoom on the outlet regions.

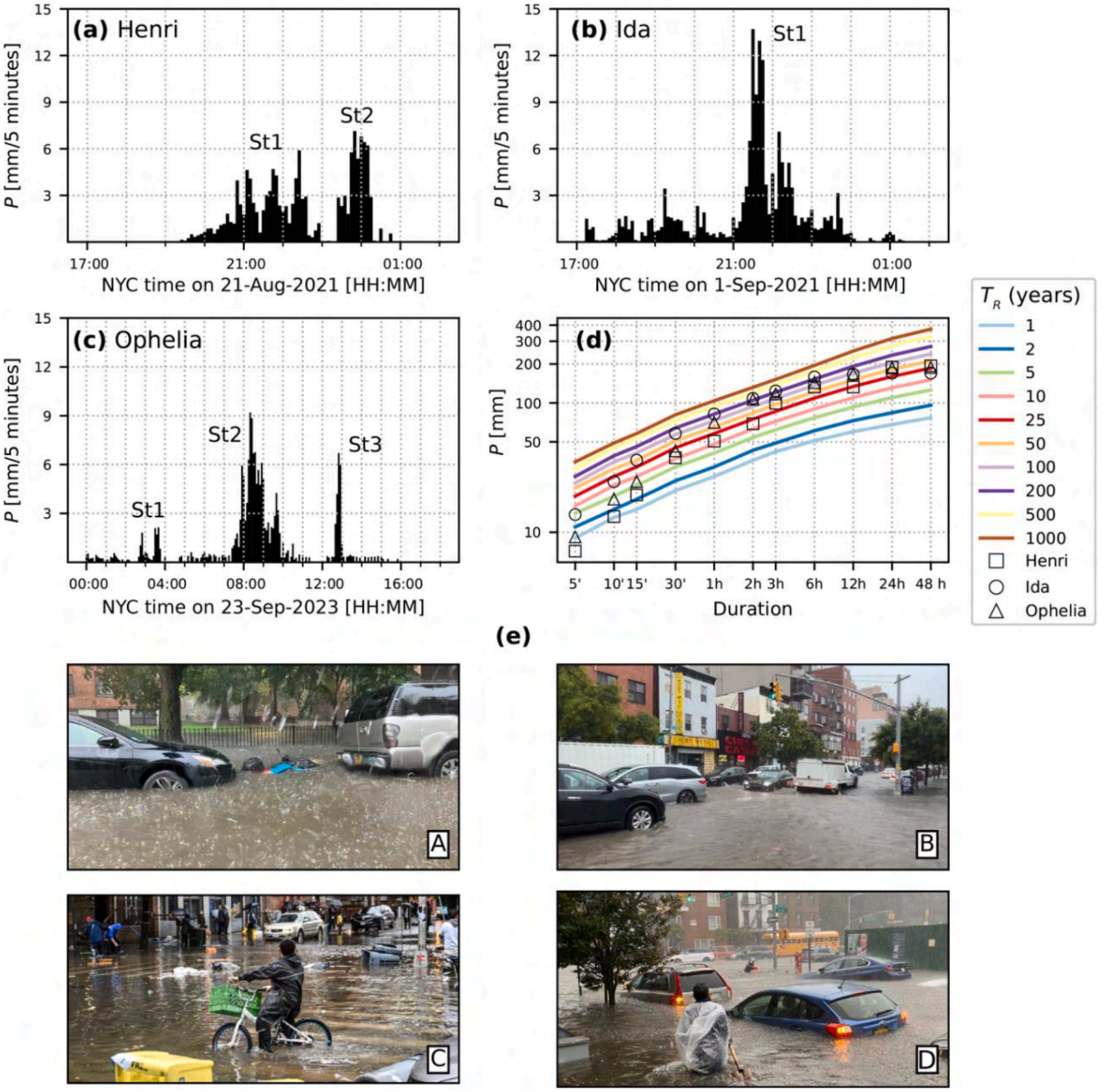

**Fig. 4.** (a)-(c) Precipitation hyetographs observed by the NYS Mesonet rain gauge during Henri, Ida, and Ophelia with labels of the main storms. (d) Intensity-duration-frequency (IDF) curves at La Guardia Airport compared with the observed maximum precipitation depths; $T_R$ is the return period. (e) Pictures of the event in locations A (Credits: Steve Kastenbaum), B (Credits: Liam Quigley), C (Credits: Fatih Aktas/Anadolu Agency via Getty Images), and D (Credits: Joann Amitrano) shown in Fig. 1c,d.

integration of a hydrologic model to reproduce rainfall–runoff processes in pervious and impervious surfaces, a hydrodynamic model to represent overland flow routing of stormwater, and a hydraulic model to capture flow routing within sewer pipes. To our knowledge, no open-source modeling system currently represents all these processes in a fully coupled and highly detailed manner.

A simpler version of this modeling scheme involves the use of coupled 2D-1D hydrologic-hydraulic models, which integrate a 2D "rain-on-grid" hydrodynamic model with a 1D pipe flow model (Cea et al., 2025; Rosenzweig et al., 2021). The rain-on-grid feature expands the capabilities of traditional hydrodynamic models designed to simulate fluvial flooding by allowing the ingestion of spatially distributed net precipitation grids, which implicitly account for rainfall-runoff transformations. The rain-on-grid option is now available in several open-source 2D hydrodynamic models, including HEC-RAS (Hydrologic Engineering Center, 2021), TELEMAC-2D (Broich et al., 2019; Hervouet, 2007), LISFLOOD-FP (Sampson et al., 2013; Shaw et al., 2021), PRIMo (Sanders and Schubert, 2019), and Iber (Bladé et al., 2014; Sanz-Ramos et al., 2025), among others. During the last few years, coupled 2D-1D models have been applied in urban areas worldwide (e.g., Bisht et al., 2016; Chen and Huang, 2024; Montalvo et al., 2024; Sañudo et al., 2020, 2025; Wu et al., 2018; Yang et al., 2023). However, they still have significant drawbacks, including the need for extensive information on the sewer network, the high computational cost, and the fact that they are mostly proprietary black-box software (Agonafir et al., 2023) with only a few open-source exceptions (e.g., Sañudo et al., 2025).

An alternative simulation strategy that overcomes these limitations relies on 2D rain-on-grid surface hydrodynamic models with simplified methods to account for the underground sewer effect, including lowering the precipitation by the rainfall rate used to design the sewer pipes (e.g., Carr et al., 2024; Oberauer and Lehmann, 2023; Rong et al., 2024; Singh et al., 2023; Yu and Coulthard, 2015) or increasing the infiltration rate artificially (Wang et al., 2018). When the stormwater inlets' locations were available, the sewer effect was also captured by creating distributed sinks at such locations where the outflow was considered either constant and equal to the maximum sewer capacity (Xing et al., 2022) or variable and determined through simplified formulas for weir or orifice flow (Chinchella et al., 2025; Gallegos et al., 2009; Palla et al., 2018). In both cases, the sewer capacity was assumed to be unlimited.

### 4.2. The LISFLOOD-FP hydrodynamic model

The hydrologic-hydraulic modeling framework adopted in this study is based on the LISFLOOD-FP 2D hydrodynamic model forced with net precipitation grids, along with different strategies to account for the sewer. The key elements of the framework and its application in the study basins are described in this and the following sections.

LISFLOOD-FP simulates surface routing dynamics of fluvial and pluvial flooding by solving the 2D shallow water equations over a regular grid using several solution schemes with different mathematical and numerical complexities (Bates et al., 2010; De Almeida et al., 2012; Hunter et al., 2005; Shaw et al., 2021). Among these, we used the FV1 scheme in version 8.1, which solves the full system of equations using a first-order finite volume method with good accuracy and computational efficiency, also because it is parallelized for use in multi-core GPU and CPU (Shaw et al., 2021). The model inputs can be time series of inflow hydrographs at specific locations and time-varying precipitation grids (Sampson et al., 2013). Among the available boundary conditions, distributed sinks can be specified along with the corresponding time series of discharge leaving the domain. Model outputs include water depth and the two horizontal components of velocity and discharge.

Buildings are key features affecting flood dynamics in urban environments; as such, approaches with different complexities, computational cost, and accuracy have been proposed to incorporate their effect in 2D hydrodynamic models (Mustafa and Szydłowski, 2021; Schubert and Sanders, 2012). The main methods are summarized in Text S1 of the Supporting Information. Among the available options in LISFLOOD-FP, we adopted the reflective-boundary approach (Bellos and Tsakiris, 2015; Chaudhry, 2008), which considers buildings as reflective boundaries, i.e., the velocity in the normal direction is reversed (or reflected) to simulate water bouncing off the obstacle, while the tangential velocity is preserved, allowing water to slide along the obstacle boundary. This method is accurate and computationally manageable compared to other simplified techniques. We implemented it by flagging the building footprints' cells as NODATA.

### 4.3. Generation of net precipitation grids

We accounted for the rainfall-runoff transformation by generating 1-m grids of net precipitation every $\Delta t = 5$ min, corresponding to the rain gauge resolution. Net precipitation was defined as precipitation minus the losses caused by canopy interception and soil infiltration. Given the relatively short duration of the storm, evaporation was considered negligible. The net precipitation between ($t$ - $\Delta t$) and $t$, $NP_t$, was computed in each pixel as:

$$NP_t = P_t - V_t - I_t, \tag{1}$$

where $P_t$ is the precipitation measured by the rain gauge, $V_t$ is the water intercepted by the tree canopy, and $I_t$ is the water infiltrated in the soil. All fluxes are cumulative depths (in mm) within $\Delta t$. The two loss terms only exist for specific land cover classes, as described next.

The losses due to canopy interception, $V_t$, were computed in the pixels classified as "tree canopy" (Fig. 3 and Table 2) based on the procedure of the i-Tree software suite from the U.S. Department of Agriculture Forest Service, described by Hirabayashi (2013). The details are given in Appendix A. Infiltration losses, $I_t$, were calculated in the pixels classified as "bare soil" and "grass/shrub" (Fig. 3 and Table 2) and in the tree pits. The locations of the latter were estimated by (1) finding the coordinates of each tree from the 2015 Street Tree Census Data point file geodatabase (Table 1), (2) verifying that the land cover class in the co-located pixel was "tree canopy," and (3) identifying three connected pixels including the pixel where the tree is located plus two of the eight adjacent pixels selected based on the orientation of the closest street. This mimics a $3 \times 1$ m$^2$ rectangular tree pit typically adopted in NYC. The infiltration was computed using the Green-Ampt scheme (Green and Ampt, 1911) implemented in the Landlab open-source Python package (Barnhart et al., 2020; Hobley et al., 2017), assuming a saturated hydraulic conductivity of $10^{-6}$ m/s, which captures the average soil types of the region (Soil Survey Staff, 2025). For the tree pits, the infiltration was computed using precipitation that does not touch the canopy and directly reaches the ground, i.e., ($P_t$ - $V_t$).

As mentioned above, the building pixels were flagged as NODATA. We accounted for the precipitation falling on the building roofs as follows. For each building, we identified the roof boundary from the building footprint dataset (Table 1) and computed the roof area, $A_{roof}$. For each time step, we calculated the precipitation volume fallen on the roof within $\Delta t$ as $V_{BR,t} = P_t \cdot A_{BR}$ and assumed that this volume instantaneously falls on the $n_{bound}$ pixels immediately outside the building perimeter. The latter were extracted by applying a buffer of 1 pixel to the roof boundary. We then assigned the same precipitation depth to each of the $n_{bound}$ pixels computed as $P_{BR,t} = \frac{V_{BR,t}}{n_{bound} \cdot A_{pixel}}$, where $A_{pixel} = 1$ m$^2$. This contribution from the roof was added to the net precipitation directly falling on the $n_{bound}$ grid points. An example of a net precipitation grid under an input of 1 mm in 5 min is reported in Fig. 5. Note the larger intensities along the roof boundaries and the lower values in trees, tree pits, and pervious areas.

### 4.4. Representation of the stormwater sewer network

We adopted two approaches to represent the effect of the sewer. The

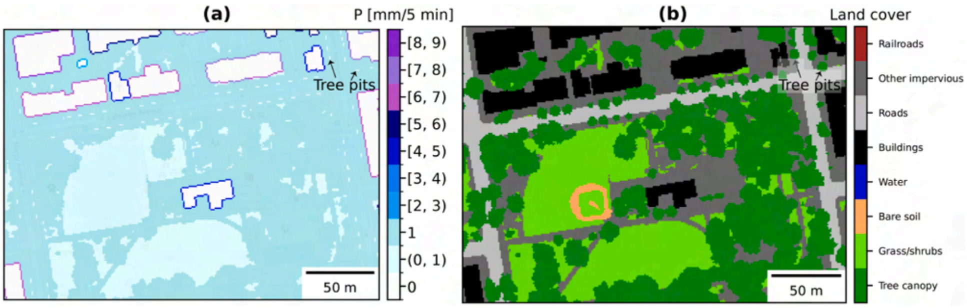

**Fig. 5.** (a) Net precipitation grid under an input of 1 mm in 5 min in a portion of the domain including multiple land cover classes (shown in panel b) and tree pits. The tree pits are located at the sides of the streets; as an example, two of them are indicated with arrows in both panels.

first assumes that the sewer can immediately absorb the runoff resulting from the precipitation intensity used to size its components, $P_{design}$. Its implementation involves replacing $P_t$ in Eq. (1) with $P_t^*$, which is defined as:

$$\begin{cases} P_t^* = P_t - P_{design} & \text{if } P_t > P_{design} \\ P_t^* = 0 & \text{if } P_t \leq P_{design} \end{cases} \tag{2}$$

This method is used by governmental agencies in the U.K. (Environment Agency, 2019) and has been adopted in different studies when detailed sewer data were unavailable (Carr et al., 2024; Singh et al., 2023; Yu and Coulthard, 2015). For NYC, we assumed $P_{design} = 44$ mm/h, corresponding to the 5-year, 1-hr storm (NYC Mayor's Office of Resiliency, 2021; Fig. 4d).

The second approach is more sophisticated and represents the drainage from each stormwater inlet according to a simplified outflow equation. We were able to implement this method thanks to the availability of the stormwater inlet locations from the OpenNYC repository (Table 1). As an example, Fig. 6 shows the inlet locations close to three FloodNet sensors, along with pictures of the typical inlet types. As part of the available boundary conditions, LISFLOOD-FP allows the specification of distributed sinks with externally provided time series of outflows. When applying this method, the outflow time series are not known in advance because they depend on the local surface water depth and velocity, which are dynamic model variables. We then modified the *fv1.cpp* file of the source code to allow the computation of the outflow in each sink, $Q_o$, as a function of the water depth, $h$, and the 2D velocity vector magnitude, $u$, in the co-located pixel at each time step. We adopted an experimental relationship among $Q_o$, $h$, and, $u$ based on the experiments of Xia et al. (2022), which reasonably captured lab measurements under three flow behaviors, including weir flow for relatively shallow water, orifice flow for relatively high water, and a critical state in between. Such a relationship is:

$$Q_o = k \cdot u \cdot A_{inlet} \cdot Fr^{\alpha}, \tag{3}$$

where $u$ is the approaching flow velocity, $A_{inlet}$ is the inlet area, and $Fr = u/\sqrt{gh}$ is the Froude number, with $g$ being the gravity acceleration, and $k$ and $\alpha$ are empirical coefficients, estimated by Xia et al. (2022) as $k = 0.302$ and $\alpha = -0.816$. In the modified source code, we used the simulated $h$ and $u$ at each time step and inlet location to compute $Q_o$ using Eq. (3), which allowed modeling stormwater removals. Given the

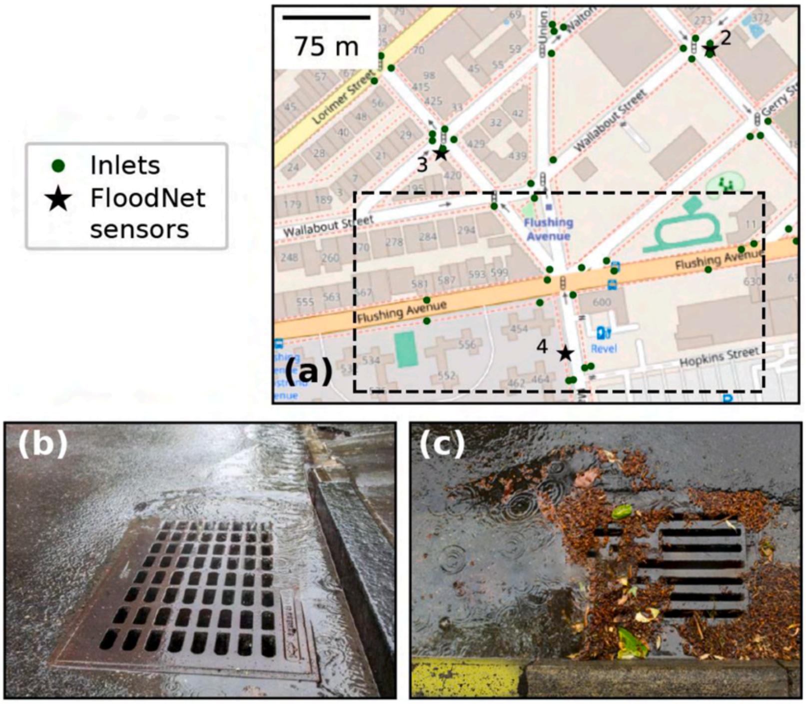

**Fig. 6.** (a) Location of stormwater inlets from the OpenNYC dataset (see Table 1) close to some FloodNet sensors. The black dashed rectangle in (a) depicts the area shown in Fig. 10. The base maps displayed in the panels are from OpenStreetMap. (b)-(c) Pictures of typical inlets in NYC in clear (credit: NYC DEP, 2021) and partially clogged (credit: NYC 311, n.d.) conditions.

variety of inlet types and clogging conditions in our basin (Fig. 6), which were unknown and whose heterogeneity could not be represented, we assumed a single set of parameters in Eq. (3) to represent all inlets. Specifically, we selected a mean value of 0.4 $\mathrm{m}^2$ for $A_{inlet}$ and the same value of $-0.816$ proposed by Xia et al. (2022) for $\alpha$, while we calibrated $k$ to simulate water depths that most closely match the FloodNet observations in the CB during Ophelia.

### 4.5. Model setup and numerical simulations

The LISFLOOD-FP computational domain for the CB consisted of a 5196 × 3620 grid centered on the basin and including a buffer of 100 cells in each direction. Elevation data provided by the LiDAR DEM (Table 1) were assigned to all grid cells except those corresponding the buildings, which were flagged as NODATA. This configuration resulted in 7,075,887 non-building cells within the basin. For the VB, the computational domain included a 1542 × 1174 grid with a buffer of 60 cells in each direction, resulting in 503,518 non-building cells within the basin boundaries.

One of the model's inputs is the grid of Manning's roughness coefficients. These values were determined based on the look-up table for the land cover classes proposed by Van Der Sande et al. (2003), except for the "tree canopy" class, which we considered as "other impervious" since the trees are located mainly in the sidewalks (see Table 2). We assigned a zero-flux boundary condition to the northern, eastern, and southern domain borders, while we prescribed as open the western border containing the watershed outlet for both basins. We considered the basins initially dry, i.e., zero water depth everywhere. The outputs were generated every 5 min, consistent with the precipitation data.

In the CB, we performed three simulations to reproduce flooding observed during Ophelia. In the first simulation, labeled No-SW, we did not represent the sewer effects and generated net precipitation grids every 5 min for 18 h (totaling 216 grids), as described in Section 4.3. We assumed the precipitation input was spatially constant within the basin using the records at the rain gauge in Fig. 1. We prescribed zero precipitation outside the basin to avoid unnecessary calculations and in agreement with the setup of zero-flux boundaries at three domain borders. In the second simulation, labeled Sim-SW, we accounted for the sewer through the simplified approach that subtracted the design storm from the observed precipitation. For this case, we created net precipitation grids as done for the No-SW experiment, with the subsequent application of Eq. (2). Finally, in the third experiment, we modeled the sewer impact using Eq. (3) with the modified LISFLOOD-FP code and the same net precipitation grids of the No-SW experiment. We conducted the third experiment, labeled Out-SW, multiple times with different values of $k$ in the outflow Eq. (3) to identify its optimal value. We also performed a sensitivity analysis on the $\alpha$ exponent in Eq. (3), without achieving improved results (not shown). Hence, due to the inherent simplifications of the adopted approach, we deemed that assuming $k$ as the only calibration parameter was adequate.

As shown in the results, the third approach led to the best performance. We extensively assessed the robustness of the Out-SW approach with $k$ determined at the CB by simulating all three precipitation events in the VB. The duration of these simulations was also 18 h. We assessed the model's ability to capture the water depths at the FloodNet sensors by computing root mean square error (RMSE), mean bias error (MBE), and Pearson's correlation coefficient (CC) between the simulated and observed water depth time series. In addition, we calculated the difference between simulated and observed peaks ($\Delta h_{peak}$) and their occurrence times ($\Delta t_{peak}$). Multiple metrics were adopted to quantify distinct components of the model performance. Since the observed water depths are available at 1-minute resolution with some gaps and the simulations are every 5 min, we obtained the simulated values at the observation times via linear interpolation. All metrics are defined in Appendix B. We also computed basin flood metrics, including total fluxes; extent of flooded areas with different depth ranges; and flooding intensity for nuisance conditions (Moftakhari et al., 2018), and low, moderate, significant, and extreme hazard levels for people, defined by the U.K. Department for Environment, Food & Rural Affairs (DEFRA, 2006; Surendran et al., 2008) based on water depth and velocity, as described in Appendix B and shown in Figure S1.

## 5. Results

### 5.1. Assessment of the three modeling approaches in the calibration basin for the Ophelia event

In the current and following sections, the simulation results are presented by comparing the time series of water depth, $h$, observed by the FloodNet sensors and simulated in the co-located 1 × 1 m pixel, and displaying the map of the maximum $h$, $h_{max}$, across the simulation duration. The error metrics at each sensor are reported in Tables S2 and S3 for the CB and VB, respectively, while the basin flood metrics are presented in Table 3.

We begin with the simulations of the Ophelia event in the CB. The $h$ time series are shown in Fig. 7. The sensors (gray lines) did not measure any standing water caused by the first main storm St1, while they all reported a hydrograph with a nonzero $h$ caused by storm St2. The increasing limb started at about 08:00, which is 30 min after the beginning of storm St2; the peak occurred between 08:51 and 09:27, depending on the sensor; and the falling limb ended at 09:25 at sensor 6 and between 10:00 and 12:08 at the other sensors. No standing water was observed after storm St3. The abrupt peak measured at sensor 2 might be due to debris floating on the water; disregarding this spike, the peaks ranged from 0.31 m to 0.65 m across the sensors.

When compared to the observations, the hydrographs simulated neglecting the sewer (No-SW; black lines) are much longer and characterized by multiple peaks and rising and falling limbs with different slopes driven by the three main storms: $h$ starts increasing early in the simulation, reaches the largest peak between 10:05 and 10:15 at all sensors, and slowly decays until the end of the simulation with a minor peak caused by storm St3 without returning to zero. The error metrics indicate poor temporal correspondence ($0.2 \leq \mathrm{CC} \leq 0.48$; Table S2), a large overall error ($0.59\ \mathrm{m} \leq \mathrm{RMSE} \leq 1.18\ \mathrm{m}$), and a severe overestimation of $h$ across the entire time series ($+0.51\ \mathrm{m} \leq \mathrm{MBE} \leq +0.93$

**Table 3**
Flood metrics for each simulation and basin, including storm durations, cumulative basin-averaged flows, and percent of the basin areas with maximum water depth ($h_{max}$) within several ranges and with different flood intensities occurring for >15 min. The latter are nuisance flooding and low, moderate, significant, and extreme hazards defined in Appendix B.

| | No-SW | Sim-SW | Out-SW | Out-SW | Out-SW | Out-SW |
|---|---|---|---|---|---|---|
| **Basin** | **CB (Area: 10.9 $\mathrm{km}^2$)** | | | **VB (Area: 0.8 $\mathrm{km}^2$)** | | |
| **Precipitation event** | Ophelia | | | Ophelia | Henri | Ida |
| **Approximate total duration of storms** | 10.4 h | | | 10.4 h | 5.1 h | 7.75 h |
| *Cumulative flows [mm]* | | | | | | |
| **Net precipitation** | 173 | 75 | 173 | 172 | 140 | 164 |
| **Surface runoff** | 173 | 75 | 33 | 51 | 43 | 53 |
| **Outflow to stormwater** | 0 | 0 | 140 | 121 | 97 | 111 |
| *Percent of the basin area in $h_{max}$ map [%]* | | | | | | |
| **$0.03\ \mathrm{m} < h_{max} \leq 0.1\ \mathrm{m}$** | 10.28 | 9.82 | 11.56 | 15.00 | 13.75 | 16.25 |
| **$0.1\ \mathrm{m} < h_{max} \leq 0.3\ \mathrm{m}$** | 7.89 | 6.79 | 6.70 | 5.00 | 5.00 | 8.75 |
| **$0.3\ \mathrm{m} < h_{max} \leq 2.0\ \mathrm{m}$** | 12.11 | 7.98 | 4.86 | 3.75 | 3.75 | 5.00 |
| **$h_{max} > 2.0\ \mathrm{m}$** | 1.19 | 0.09 | 0.09 | 0.25 | 0.13 | 0.25 |
| *Percent of the basin area with flood intensity lasting for >15 min [%]* | | | | | | |
| **Nuisance flooding** | 26.88 | 18.35 | 20.83 | 25.00 | 21.25 | 30.00 |
| **Low hazard** | 18.17 | 10.92 | 10.46 | 10.00 | 7.50 | 11.25 |
| **Moderate hazard** | 11.74 | 6.06 | 5.05 | 3.75 | 2.50 | 5.00 |
| **Significant hazard** | 13.30 | 7.16 | 4.04 | 5.00 | 3.75 | 5.00 |
| **Extreme hazard** | 3.58 | 1.19 | 0.73 | 1.25 | 1.25 | 1.25 |

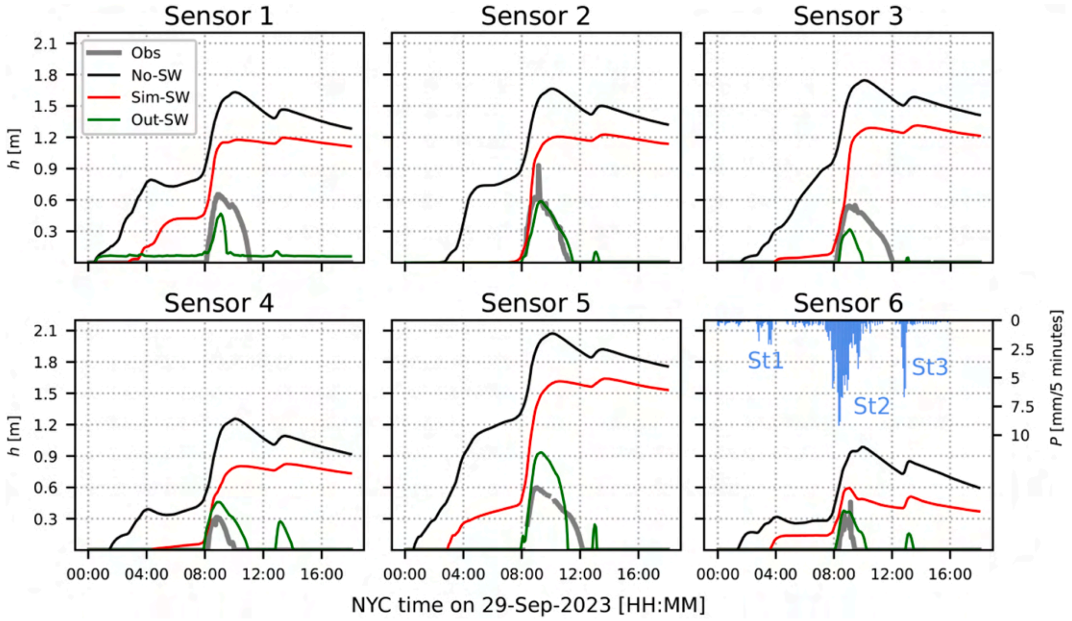

**Fig. 7.** Time series of water depth, *h*, observed and simulated with the three approaches at six FloodNet sensors in the CB during Ophelia. For reference, the precipitation hyetograph is reported in the panel of sensor 6, along with the storms' labels.

m) and of the peaks ($+0.53$ m $\leq \Delta h_{peak} \leq +1.48$ m), which are simulated with significant delays ($+43$ min $\leq \Delta t_{peak} \leq +83$ min).

Before focusing on the simulated $h_{max}$, we note that, in all three simulation approaches, we found the presence of very high *h* (even exceeding 3 m) in a small number of isolated pixels in depressions that are either garages or low-lying areas most likely drained by pumps or caused by errors in the DEM (see discussion in Section 6.3). These outliers were identified and excluded from the flooded area computation with negligible effects on the results. The map of $h_{max}$ for No-SW in Fig. 8a shows significant flooding in two large regions in the middle of the domain and close to the outlet, as well as in several streets. Specifically, $h_{max}$ exceeded 0.3 m – the flooding threshold adopted by FEMA (2018) and Schubert et al. (2024) – in 13.3% of the basin and even 2 m in a non-negligible portion (Table 3). The combined analysis of *h* and *u* also revealed that neglecting the sewer led to the simulation of moderate-to-extreme flood hazard conditions in almost a third of the basin.

When the sewer is implicitly considered in the net precipitation (Sim-SW; red lines in Fig. 7), the simulation of the hydrographs' first part dramatically improves compared to the No-SW experiment, as it leads to significantly lower *h* before 8:00 while still capturing the observed steep increase occurring at that time. Despite these enhancements, *h* is still overestimated after 8:00, even if to a lower extent than No-SW, and remains practically constant after the peak caused by storm St2 due to the lack of water losses. This is reflected in lower mean errors (0.32 m $\leq$ RMSE $\leq$ 0.89 m) and biases ($+0.27$ m $\leq$ MBE $\leq +0.62$ m) compared to No-SW; however, the temporal correspondence remains poor ($0.10 \leq$ CC $\leq 0.39$; see Table S2). For Sim-SW, the peaks are overestimated everywhere ($+0.13$ m $\leq \Delta h_{peak} \leq 1.05$ m) and are also modeled with a significant delay ($+262$ min $\leq \Delta h_{peak} \leq +297$ min), except for sensor 6 ($\Delta h_{peak} = -3$ min), because the highest simulated *h* occurs after storm St3 instead of storm St2. The map of $h_{max}$ for Sim-SW in Fig. 8b shows lower values throughout the basins compared to No-SW, with $h_{max} > 0.3$ m in 8.1% of the basin area and exceeding 2.0 m at a negligible number of pixels (Table 3). The areas under moderate to extreme hazard are about half the size of those simulated in the No-SW scenario.

To address the limitations of No-SW and Sim-SW, we modeled the sewer effect through distributed sinks located at the stormwater inlets (Out-SW). We preliminarily calibrated the parameter *k* of the outflow Eq. (3). Fig. 9 summarizes the error metrics for the simulations with four

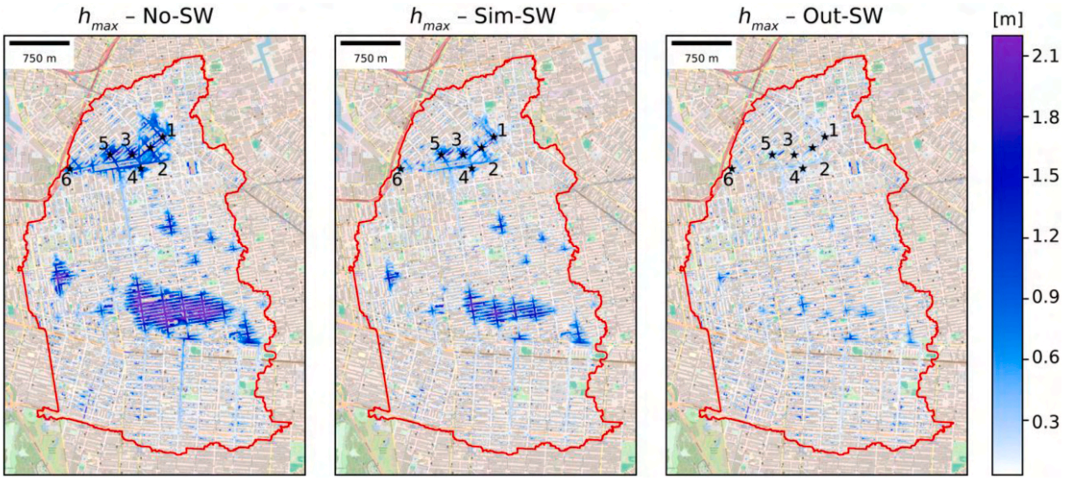

**Fig. 8.** Maps of maximum *h*, $h_{max}$, with the sensors' location in the CB for the three simulation approaches. The base map is from OpenStreetMap.

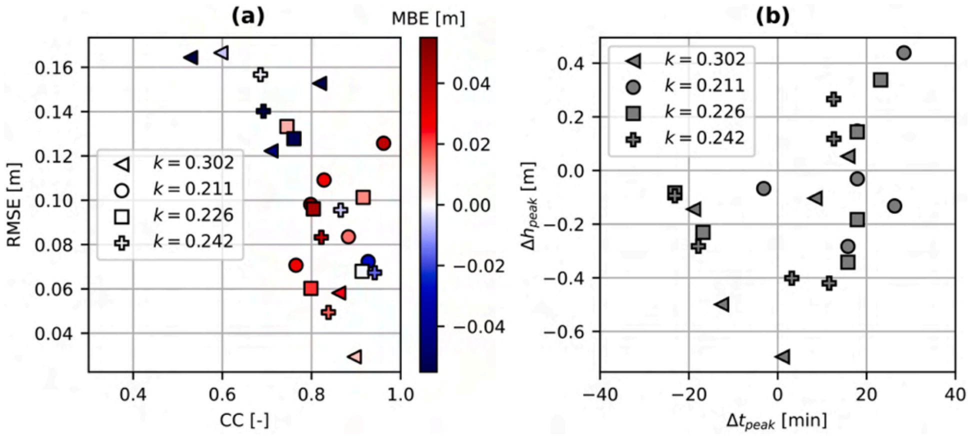

**Fig. 9.** Scatterplots between the metrics quantifying the ability to simulate (a) the entire time series and (b) the peaks at the six FloodNet sensors for the Out-SW simulations in the CB with different values of the coefficient $k$ in Eq. (3). The metrics are defined in Appendix B.

values of $k$ at the six FloodNet sensors. We started with the same value of $k = 0.302$ used by Xia et al. (2022) and found that the outflows from the basin were too high. We then repeated the simulations with $k$ reduced by 20%, 25%, and 30% and found that $k = 0.226$ (25% reduction) led to the best performances at most stations. The Out-SW simulations with $k = 0.226$ (green lines in Fig. 7) capture the observed hydrographs remarkably well, including timing ($0.74 \leq \text{CC} \leq 0.92$; Table S2), shape and magnitude of rising and falling limbs ($0.05\ \text{m} \leq \text{RMSE} \leq 0.13\ \text{m}$; $-0.001\ \text{m} \leq \text{MBE} \leq -0.05\ \text{m}$), and peaks ($-0.34\ \text{m} \leq \Delta h_{peak} \leq +0.34\ \text{m}$; $-23\ \text{min} \leq \Delta t_{peak} \leq +23\ \text{min}$). The only exceptions are a small minor peak following storm St3 at all sites. The map of $h_{max}$ in Fig. 8c looks realistic, as this variable is mainly below 0.80 m, and the two large regions with widespread flooding simulated by No-SW and Sim-SW do not appear anymore. The areas under moderate and significant hazards are further reduced, while extreme hazard conditions are almost negligible (Table 3).

### 5.2. Spatiotemporal dynamics of simulated water depths

We further demonstrated the fidelity and high level of detail of the Out-SW simulations by presenting in Fig. 10 maps of $h$ in the vicinity of sensor 4 for six times from 8:00 to 10:30 on September 29, 2023, along with the stormwater inlet location. This is the area shown with a dashed rectangle in Fig. 6a, centered at the major intersection between Flushing Avenue and Union Avenue. At 8:00, the area is largely dry except for a few localized depressions where $h$ exceeds 2 m, which are indicated to

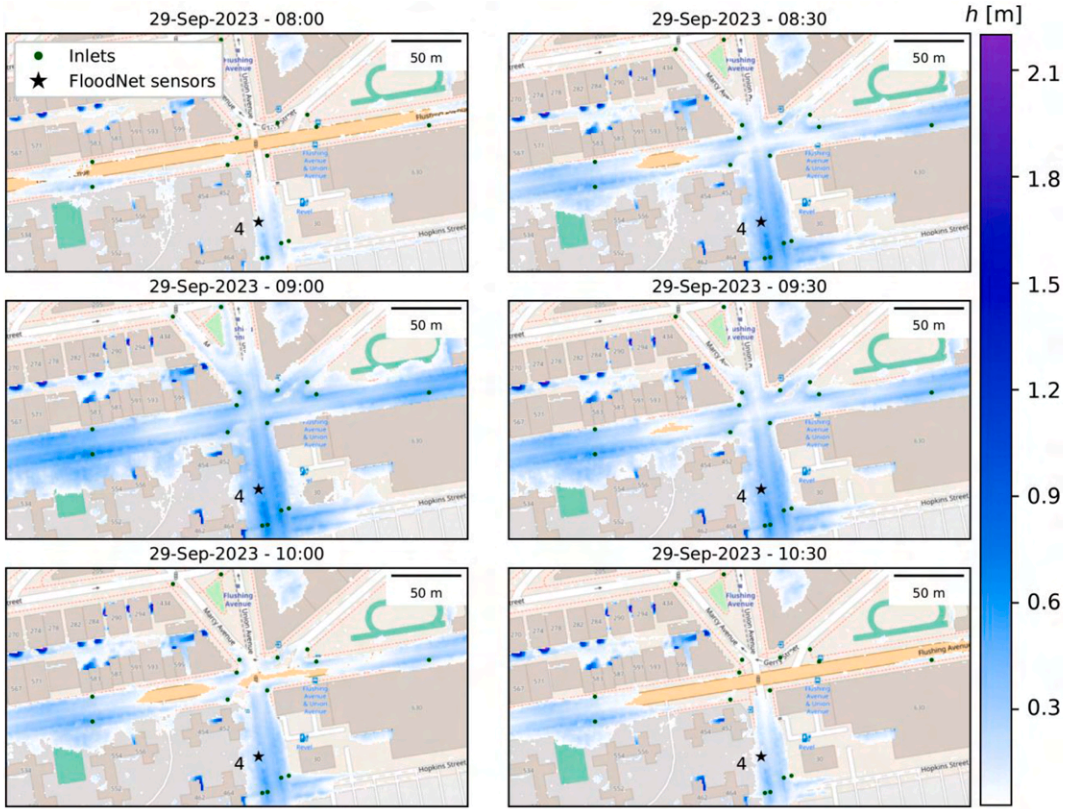

**Fig. 10.** Maps of $h$ simulated by Out-SW at six times between 8:00 and 10:30 on 29 September 2023 in the CB area depicted in Fig. 6a, with locations of the FloodNet sensor 4 and stormwater inlets. The base map is from OpenStreetMap.

be basements according to visual inspection of satellite photos. After storm St2 begins, water starts ponding on the roadways, and the flooded areas expand from 8:30 to 9:00. As the precipitation intensity decreases after 9:00, the flooded areas recede because water enters the stormwater inlets, as illustrated in the maps for 9:30, 10:00, and 10:30. Note how the larger number of inlets placed at the major intersection leads to a faster contraction of the flooded area compared to the regions located ~50 m away that are drained by a smaller number of inlets, including where sensor 4 is located. The maps of Fig. 10 also demonstrate that the reflective-boundary method implemented in LISFLOOD-FP represents the water flow around the buildings very well. An animation of this simulation is available in Movie S1 of the Supporting Information.

### 5.3. Transferability of the best-performing simulation approach

The Out-SW modeling approach performed very well in the CB, after the $k$ value in Eq. (3) was calibrated against the FloodNet $h$ observations. We tested the robustness of this approach in the VB during all three precipitation events using $k$ from the CB. Results are shown in Fig. 11, and the error metrics are reported in Table S3. The Out-SW simulations reproduce very well the hydrographs' timing ($0.54 \leq \text{CC} \leq 0.98$), magnitude ($0.04 \text{ m} \leq \text{RMSE} \leq 0.15 \text{ m}$; $-0.002 \text{ m} \leq \text{MBE} \leq -0.003 \text{ m}$), and shape ($-0.35 \text{ m} \leq \Delta h_{peak} \leq -0.09 \text{ m}$; $5 \text{ min} \leq \Delta t_{peak} \leq +140 \text{ min}$) for all three events. Notably, the model accurately captures the differences in $h$ peaks measured at sensors 7 and 8 during Ophelia, which are significant despite the proximity of these sites. In addition, the model almost perfectly reproduces the hydrograph caused by Ida. There are two instances where the performance of Out-SW is lower: the model (1) cannot reproduce the first observed peak caused by storm St1 during Henri (note also the presence of a spike likely caused by a floating object), and (2) simulates a second minor peak during Ophelia that was not observed. We carefully investigated the possible causes for these errors and concluded that the most plausible is the use of precipitation measurements from a rain gauge 3 km away from the basin, which may not accurately represent the precipitation that occurred in the basin during these times. Despite these two instances of lower performance, the comparisons with street flooding observations provide strong confidence in the robustness of the calibrated approach.

As a final note, the maps of $h_{max}$ are similar across all events (the map for Ida is shown in Fig. 11, the CC among the maps is $> 0.99$), with higher values in the back of the buildings and the downstream area close to the sensors. This is reflected in the close values across the three events of the flood metrics reported in Table 3. It is worth noting that, despite differences in terrains, the percentages of the basin area in different flooding conditions in the CB and VB are also quite similar. The figure for the VB corresponding to Fig. 10 and an animation of the water depth spatiotemporal dynamics during the three storms are reported in Figures S11-S13 and Movies S2-S4.

## 6. Discussion

### 6.1. The value of street flooding observations to assess flood modeling approaches

The accurate simulation of pluvial flooding at hyperlocal scales is a challenging task influenced by several sources of uncertainty (Bates, 2023). A key step in reducing this uncertainty and building confidence in simulations of urban flood dynamics is their validation against distributed, continuous street flooding observations (Cea et al., 2025; Molinari et al., 2019; Schubert et al., 2024). Such measurements are not yet routinely collected anywhere in the world, with the notable exception of the FloodNet network in NYC (Mydlarz et al., 2024). Here, we used data from this observational network to perform what we believe is the first assessment of this kind for three popular modeling approaches used in the literature. To capture small-scale flood dynamics in heterogeneous urban regions and enable meaningful direct comparison with the sensor footprint, we applied the model at the hyperlocal resolution of 1 m$^2$.

The novelty of our assessment lies in the use of spatially distributed, continuous, street-level water depth observations to evaluate both the magnitude and timing of simulated pluvial flood dynamics. Previous validation efforts have typically relied on static indicators such as maximum flood extents or water marks, event-integrated metrics, or proxy datasets, which do not capture the temporal evolution of flooding and therefore limit the ability to discriminate among competing modeling approaches. By contrast, the FloodNet observations enable a quantitative, time-resolved evaluation of model performance at hyperlocal scales, allowing us to identify strengths and limitations of commonly adopted sewer-representation strategies that would not be evident from spatial-only validations.

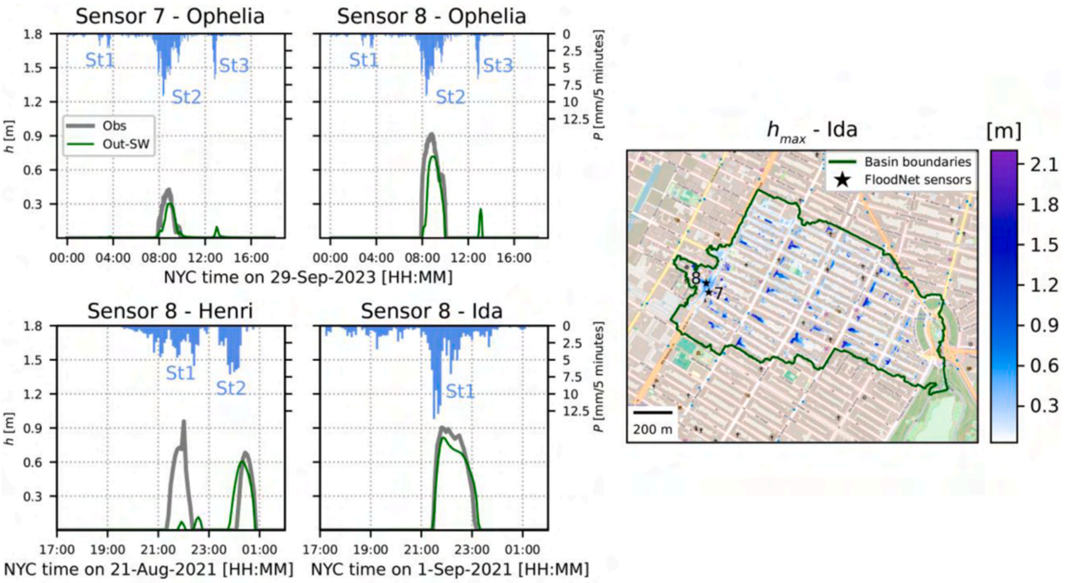

**Fig. 11.** Results of the Out-SW simulations for the VB. Left panels: time series of observed and simulated $h$ at the FloodNet sensors 7 and 8 during Ophelia and sensor 8 during Ida and Henri; the precipitation hyetographs and the storms' labels are also reported in each panel. Right panel: map of $h_{max}$ during Ida. The base map is from OpenStreetMap.

The study was conducted in two flood-prone basins of different sizes and topographic features. The three simulation approaches were assessed in the CB against water levels from six FloodNet sensors observed during the Ophelia event. Some studies assumed that, under intense storms like Ophelia (Fig. 4d), the sewer network quickly reaches its capacity and does not significantly impact the extent and severity of flooding hazards (Ivanov et al., 2021; Schmitt and Scheid, 2020). However, our simulations indicate that neglecting the sewer (No-SW) leads to severe overestimations of the extent and severity of flooding hazards (Table 3), which appear too large even for a conservative assessment. These findings align with Kasaei et al. (2025), who simulated pluvial and coastal flooding from Hurricanes Ida and Ophelia in Jamaica Bay, NYC, using the COAWST model at a moderate spatial resolution (~50 m). Their simulations that did not account for the sewer system overestimated the observed high-water marks. Our overestimations are also consistent with other studies that compared a simulation without the drainage sewer against either $h_{max}$ observations (Xing et al., 2022), coupled 2D-1D simulations (Montalvo et al., 2024), or 2D simulations with a simplified sewer, as in our Out-SW scenario (Schubert et al., 2024).

The simplified method that implicitly incorporates the sewer by reducing the net precipitation (Sim-SW) has been suggested by national design standards in the U.K. (Environment Agency, 2019) and applied in several studies with reductions that were either spatiotemporally constant (Montalvo et al., 2024; Yu and Coulthard, 2015), spatially variable and temporally constant (Carr et al., 2024; Singh et al., 2023), spatially constant and temporally variable (Oberauer and Lehmann, 2023), or spatiotemporally variable (Li et al., 2020). Our comparison with observed $h$ in the CB reveals that applying a spatiotemporally constant reduction has some skill in modeling the initial volume entering the sewer. This is consistent with the abovementioned study by Kasaei et al. (2025), where significant improvements were achieved by considering a spatially constant drain rate of 13 mm/h. However, this approach still importantly overestimates all flooding variables, leading to spatial patterns of $h_{max}$ that are not too different from No-SW (Table 3). This outcome is opposite to what was found by Xing et al. (2022), who reported underestimations of the precipitation reduction method in a dense urban basin in Fuzhou, China. Focusing on a 0.6-km$^2$ basin in Spain, Montalvo et al. (2024) reported instead that reducing the precipitation rate led to both over- and under-estimations of $h$ in different basin areas compared to a coupled 2D-1D simulation. In the future, the availability of longer records of street flooding observations could be very valuable in identifying and calibrating the optimal reduction of precipitation rates in space and time, eventually combined with increased infiltration rates. After proper calibration, this approach will likely be more data parsimonious and computationally efficient than other modeling techniques.

The approach where the drainage system is modeled through distributed sinks at the stormwater inlet locations (Out-SW) led to very good performances at all sensors in the CB, after calibrating only one parameter ($k$ in Eq. (3)) against the observations. The availability of $h$ measurements in another basin (the VB) gave us strong confidence that this calibrated approach is robust and transferable in dense urban areas in NYC. We argue that the robustness observed across basins and events is primarily driven by the physically based structure of the model and its application at hyperlocal scales, which allow local water depth and flow velocity at stormwater inlets to be simulated with sufficient fidelity to reliably estimate inlet outflow. The identification of the specific value of the calibrated outflow parameter $k$ plays a secondary role, but it remains necessary to successfully reproduce the observed hydrographs. The parameter $k$ implicitly aggregates site-specific factors such as inlet geometry, maintenance condition, and partial clogging, which may vary across cities or even within a single urban area. As such, while the results indicate that the proposed approach is transferable within dense urban environments with broadly similar drainage characteristics, additional calibration may be required when applying the method to regions with substantially different inlet designs, maintenance regimes, or hydrologic conditions.

These considerations are supported by Schubert et al. (2024), who demonstrated the superiority of a simplified inlet-based method in Los Angeles, a city that is significantly less dense than NYC. These authors performed regional flood simulations with a strategy, named PRIMo-Drain, where stormwater runoff was removed at over 150,000 inlets using a weir and orifice relationship based on a single coefficient, which was calibrated to contain flood inundation within street curbs for the 20-year storm. The PRIMo-Drain simulations were deemed more realistic than other modeling approaches that did not incorporate the sewer pipes. On the other hand, the abovementioned study by Xing et al. (2022) applied a method similar to Out-SW by assuming a constant outflow based on local stormwater design standards at inlets identified from street view images. The simulations were compared against observations of $h_{max}$ during two storms, finding only moderate improvements compared to a scenario that did not consider the sewer. The superior performance of the Out-SW simulations shown here could be attributed to (1) the use of dynamic outflow rates that change with the flow conditions and (2) the comparison against time-varying observed $h$.

### 6.2. *Insights into model setup in complex urban basins*

Our modeling effort provides valuable insights for setting up and applying flood models in complex urban regions at hyperlocal resolutions. Some of these details might have already been mentioned in the literature but relatively sparsely. Therefore, we believe that summarizing them is helpful for researchers and practitioners interested in applying flood models to advance the knowledge of pluvial flooding and design mitigation strategies. (1) Digital elevation models should be “hydroenforced”, i.e., modified to remove the effect of elevated infrastructure that could erroneously obstruct water flow. (2) Depressions in high-resolution DEMs should be kept when deriving the basin boundaries. However, as described in the next section, depression outliers should be inspected as they could be caused by errors in the DEM and might need to be removed while post-processing model outputs. (3) The reflective boundary method led to a realistic simulation of the water flow around buildings, a key modeling capability in dense urban regions. In LISFLOOD-FP, this method is applied by setting the building cells to NODATA. (4) Rain-on-grid hydrodynamic models might not include rainfall-runoff transformation. Here, we proposed a framework to generate net precipitation grids that account for the losses caused by canopy interception and soil infiltration and the precipitation redistribution around the building roofs. Python codes have been made publicly available (see Software availability statement).

### 6.3. *Limitations and future work*

Inevitably, our simulations also have limitations and inaccuracies. All modeling approaches tested here produced high water depths in localized areas, which were deemed to be unrealistic. These cases are primarily located in depressions, identified by subtracting the DEM from its filled version (Figure S2). We inspected satellite imagery and street-view pictures to verify the source of these depressions and found two main groups. The first includes cases where the depressions are playgrounds, parking areas, basements, and railroads located at lower elevations than the surrounding streets or sidewalks (see examples in Figures S3-S7); in these cases, it might be possible that pumping stations or inlets not included in the city database drain these low-lying areas. In the second group of cases, the pictures did not reveal any important elevation differences, suggesting that the depression could be due to errors in the DEM or the absence of buildings that are present in the city database (see examples in Figures S8-S10).

While precipitation spatial variability can influence urban flood dynamics, our modeling applications targeted only the uncertainties associated with hydraulic routing and sewer representation, rather than precipitation forcing. The net precipitation forcings of our runs were obtained assuming spatially uniform precipitation from a rain gauge outside the basins' boundaries. Since the catchments have small areas and are within 3 km from the gauge, this assumption led to good performance in most cases. The only exception was a missed peak caused by St1 during Henri in the VB, which we ascribed to the rain gauge records underestimating the actual precipitation in the basin. Future efforts should focus on generating more accurate precipitation fields that capture localized high rain rates and the spatial variability of intense storms that are often the main drivers of urban flash floods (Ochoa-Rodriguez et al., 2015; Peleg et al., 2022; Zhou et al., 2021). Such an effort will require sub-kilometer and sub-hourly gridded precipitation fields, which in NYC could be obtained from weather radars (e.g., Zhang and Gourley, 2018) after accounting for their uncertainty, as done by Hjelmstad et al. (2021) in Phoenix, AZ. Given its good performance, the hydrologic-hydraulic model proposed here could also be used to investigate whether storms characterized by different precipitation spatiotemporal variability, either observed or simulated by stochastic models (Hartke et al., 2022; Mascaro et al., 2023; Papalexiou et al., 2021; Peleg et al., 2017), have distinct impacts on urban flooding.

The approach adopted to account for the precipitation falling on the building roofs is simplified since it does not consider (1) the time lag in precipitation arrival from the roof to the ground, which is affected by building height and roof type; (2) the possible presence of downspouts, which implies a non-uniform contribution along the building perimeter; and (3) the direct discharge of precipitation water from the roof to the sewer via the downspouts, which occurs in several NYC buildings (NYC Mayor's Office of Resiliency, 2021). We believe these limitations are acceptable in this phase and should be addressed in future work, especially considering that the latter two could only be overcome by adopting a 2D-1D model that explicitly represents the sewer.

All methods adopted here do not consider or strongly simplify the sewer effect. The best-performing Out-SW method assumes infinite sewer capacity and cannot represent surcharging and overflowing conditions. Therefore, the proposed approach is most appropriate for simulating events in which inlet capture dominates surface water removal, while it may underestimate flooding severity under conditions of sewer surcharge. Moreover, Out-SW also uses a single analytical form and parameterization of the outflow equation for all inlet types and clogging conditions. Future experimental work could enhance the physical representation of inlet discharge under varying configurations and operating conditions. Moreover, recent aerial images could characterize the spatial heterogeneity of inlet types and correct possible inaccuracies in the city stormwater inlet dataset.

Finally, future work should further assess the value of the simplified methods to represent the sewer, buildings, and rainfall-runoff transformations using coupled 2D-1D models validated against street flooding observations as the reference. On the one hand, coupled models are becoming increasingly available with open-source licenses (Hydrologic Engineering Center, 2024; Sañudo et al., 2025) at lower computational costs, thanks to codes running on GPUs. On the other hand, sensors monitoring street-level flooding observations are starting to be installed at other sites (Gold et al., 2023; Son et al., 2023). Tests based on coupled models should be conducted primarily when information on the sewer layout is available. If this is not the case, like in NYC, these simulations could apply recent methods proposed to generate virtual sewer networks from terrain, building, and street information (Chegini and Li, 2022; Montalvo et al., 2024).

## 7. Conclusions

The lack of street-level flooding data in urban areas has severely limited our ability to build confidence in hydrologic–hydraulic models that simulate pluvial flooding at hyperlocal resolutions, which are essential for accurately quantifying and mitigating flood hazards. In this study, we addressed this gap using continuous, spatially distributed water depth observations from the FloodNet network, which began operation in NYC in 2021. We first compared three modeling strategies using the LISFLOOD-FP two-dimensional, rain-on-grid hydrodynamic model applied at 1-m resolution to a 10.9-km$^2$ basin (CB) during Tropical Storm Ophelia in 2023. We showed that excluding the sewer network or simplifying its representation through reduced precipitation inputs resulted in significantly higher simulated water depths than observed at six sites. In contrast, the observed hydrographs were reproduced remarkably well when runoff removal at stormwater inlets was represented through an outflow relationship, with its single coefficient calibrated against the sensor measurements. We validated the robustness of this calibrated approach in a 0.8-km$^2$ basin (VB) with similar urban density but steeper terrain, using observations from two sensors during the same event and during Tropical Storm Henri and Hurricane Ida in 2021.

Our results demonstrate that street-level flooding observations are essential for calibrating, testing, and improving existing and emerging methods to model urban flooding under varying levels of data availability. In addition, we developed methodological procedures and provided guidance for preprocessing geospatial data, setting up the model domain, and generating net precipitation forcings, which can facilitate hyperlocal flood simulations in other urban landscapes. Overall, the findings of this study provide valuable insights for researchers and agencies seeking to apply hydrologic–hydraulic models to evaluate infrastructure and urban planning strategies for flood risk reduction.

## Open research

### Software availability statement

Version 8.1 of the LISFLOOD-FP software is available through its Zenodo platform at LISFLOOD-FP Developers (2022). The Python code used to produce the net precipitation, the modified *fv1.cpp* file, and the LISFLOOD-FP model setup in the study basins are available at http://www.hydroshare.org/resource/6cf42a4b61404099a3732147689f54b6 (Mascaro, 2025).

## Data availability statement

The geospatial datasets used to set up LISFLOOD-FP in the study basin are publicly available from New York City's OpenData repository at https://opendata.cityofnewyork.us (City of New York, 2025), while the Hydroenforced DEM from the NOAA website https://www.fisheries.noaa.gov/inport/item/64734 (OCM Partners, 2017). The precipitation data are available upon request to the New York State (NYS) Mesonet website: https://nysmesonet.org/about/data (Brotzge et al., 2020). The FloodNet data can be downloaded at https://www.floodnet.nyc/methodology (Mydlarz et al., 2024).

## CRediT authorship contribution statement

**S. Annis:** Writing – review & editing, Writing – original draft, Visualization, Validation, Software, Resources, Methodology, Investigation, Formal analysis, Data curation, Conceptualization. **M.G. Badas:** Writing – review & editing, Writing – original draft, Supervision, Project administration, Methodology, Investigation, Funding acquisition, Formal analysis, Conceptualization. **G. Mascaro:** Writing – review & editing, Writing – original draft, Visualization, Validation, Supervision, Software, Project administration, Methodology, Investigation, Funding acquisition, Formal analysis, Conceptualization.

## Declaration of competing interest

The authors declare the following financial interests/personal relationships which may be considered as potential competing interests: Giuseppe Mascaro reports financial support was provided by National Science Foundation. Maria Grazia Badas reports financial support was provided by European Union. Stefano Annis reports financial support was provided by European Union.

## Acknowledgments

We thank two reviewers for their constructive comments, which helped to improve the manuscript quality. S. Annis and M. G. Badas acknowledge financial support from the GeoSciences IR project IR0000037 funded by the PNRR – European Union – NextGenerationEU. G. Mascaro thanks funding from the U.S. National Science Foundation (NSF) awards #2212702: "CAS-Climate: A Novel Process-Driven Method for Flood Frequency Analysis Based on Mixed Distributions" and #2435015: "Planning: CHIRRP: Utility of Hyperlocal Flood Data to Co-Advance Urban Flood Knowledge and Mitigation Solutions with Multiple Stakeholders". G. Mascaro thanks Dr. Andrea Silverman, Dr. Charlie Mydlarz, and Dr. Debra Laefer for sharing insights about the FloodNet data and the study basin. The authors also thank the New York State (NYS) Mesonet for providing the precipitation data. Original funding for the NYS Mesonet (NYSM) buildup was provided by Federal Emergency Management Agency grant FEMA-4085-DR-NY. The continued operation and maintenance of the NYSM is supported by National Mesonet Program, University at Albany, Federal and private grants, and others.

## Supplementary materials

Supplementary material associated with this article can be found, in the online version, at doi:10.1016/j.advwatres.2026.105223.

## Appendix A: Computation of canopy interception

We computed the losses due to canopy interception in the pixels classified as "tree canopy" by adapting the procedure of the i-Tree software suite from the U.S. Department of Agriculture Forest Service, which is described by Hirabayashi (2013). Let $P_t$ be the precipitation depth fallen between ($t$ - $\Delta t$) and $t$. The method separates $P_t$ as follows:

$$P_t = V_t + Pt_t, \tag{A1}$$

where $V_t$ is canopy precipitation or the fraction of $P_t$ that falls on and touches the canopy, and $Pt_t$ is the through canopy precipitation or the part of $P_t$ that does not touch the canopy and reaches the ground directly. $V_t$ contributes to filling the canopy storage, whose maximum value is estimated as:

$$Sv_{max} = S_L \cdot LAI, \tag{A2}$$

where $S_L$ is the specific leaf storage of water, assumed equal to 0.2 mm; and LAI is the leaf area index, taken as 2 $m^2/m^2$ based on the averages across tree types in NYC. We implemented an algorithm that keeps track of the water stored in the canopy over time, $Sv_t$, by applying the mass balance without including any evaporation term, given the short duration of the storm. When $Sv_t < Sv_{max}$, then $V_t > 0$. As the storage fills, we might have a time when $Sv_t \geq Sv_{max}$; then, $Sv_t$ is set equal to $Sv_{max}$ and $V_t = (Sv_{max} - Sv_{t\text{-}1})$. When the storage is full, $Sv_t = Sv_{max}$ and $V_t = 0$.

## Appendix B: Error and flood metrics

The error metrics used to compare observed and simulated time series of water depth introduced in Section 4.5 are defined in the following equations:

$$\mathrm{CC} = \frac{\sum_{j=1}^{n}\left(h_{s,j} - \overline{h}_s\right)\cdot\left(h_{o,j} - \overline{h}_o\right)}{\sqrt{\sum_{j=1}^{n}\left(h_{s,j} - \overline{h}_s\right)^2 \cdot \sum_{j=1}^{n}\left(h_{o,j} - \overline{h}_o\right)^2}}, \tag{B1}$$

$$\mathrm{RMSE} = \sqrt{\frac{\sum_{j=1}^{n}\left(h_{s,j} - h_{o,j}\right)^2}{n}} \tag{B2}$$

$$\mathrm{MBE} = \sum_{j=1}^{n}\frac{\left(h_{s,j} - h_{o,j}\right)}{n} \tag{B3}$$

$$\Delta t_{peak} = \left(t_{p,s} - t_{p,o}\right) \tag{B4}$$

$$\Delta h_{peak} = \left(h_{p,s} - h_{p,o}\right), \tag{B5}$$

where $h_{s,j}$ and $h_{o,j}$ are the simulated and observed water depths, respectively, at time $j = 1, \ldots, n$, with $n$ being the total number of times when the observation was available; $\overline{h}_s$ and $\overline{h}_o$ are the corresponding averages; and $t_{p,s}$ and $t_{p,o}$ are the times of the simulated ($h_{p,s}$) and observed ($h_{p,o}$) peaks, respectively.

We quantified flood conditions in the basin by computing the pixels under different conditions of water depth, $h$, and flow velocity, $u$. These include nuisance flooding, defined as 0.03 m $< h \leq$ 0.10 m and $u <$ 3 m/s following Moftakhari et al. (2018); and low, moderate, significant, and extreme hazards, which were computed based on the hazard rating ($HR$) formula proposed by DEFRA (2006) and Surendran et al. (2008) as $HR = h \cdot (u + 0.5)$

$+ DF$, where $DF$ is the debris factor assumed equal to 0.5 if $h < 0.25$ and 1 otherwise; the hazard is low when $HR < 0.75$, moderate when $0.75 \leq HR < 1.25$, significant when $1.25 \leq HR < 2$, and extreme when $HR \geq 2$ (see Figure S1). Low hazard suggests that caution should be exerted for the presence of shallow flowing water or deep standing water, while moderate, significant, and extreme hazards refer to areas that are dangerous for children, most people, and all people (including emergency crews), respectively.

## References

Agonafir, C., Lakhankar, T., Khanbilvardi, R., Krakauer, N., Radell, D., Devineni, N., 2023. A review of recent advances in urban flood research. Water Secur. 19, 100141. https://doi.org/10.1016/j.wasec.2023.100141.

Barnhart, K.R., Hutton, E.W.H., Tucker, G.E., Gasparini, N.M., Istanbulluoglu, E., Hobley, D.E.J., et al., 2020. Short communication: landlab v2.0: a software package for Earth surface dynamics. Earth Surf. Dyn. 8 (2), 379–397. https://doi.org/10.5194/esurf-8-379-2020.

Bates, P., 2023. Fundamental limits to flood inundation modelling. Nat. Water 1 (7), 566–567. https://doi.org/10.1038/s44221-023-00106-4.

Bates, P.D., Horritt, M.S., Fewtrell, T.J., 2010. A simple inertial formulation of the shallow water equations for efficient two-dimensional flood inundation modelling. J. Hydrol. 387 (1–2), 33–45. https://doi.org/10.1016/j.jhydrol.2010.03.027.

Bates, P.D., De Roo, A.P.J., 2000. A simple raster-based model for flood inundation simulation. J. Hydrol. 236 (1–2), 54–77. https://doi.org/10.1016/S0022-1694(00)00278-X.

Bellos, V., Tsakiris, G., 2015. Comparing various methods of building representation for 2D flood modelling In built-up areas. Water Resour. Manag. 29 (2), 379–397. https://doi.org/10.1007/s11269-014-0702-3.

Bisht, D.S., Chatterjee, C., Kalakoti, S., Upadhyay, P., Sahoo, M., Panda, A., 2016. Modeling urban floods and drainage using SWMM and MIKE URBAN: a case study. Nat. Hazards 84 (2), 749–776. https://doi.org/10.1007/s11069-016-2455-1.

Bladé, E., Cea, L., Corestein, G., Escolano, E., Puertas, J., Vázquez-Cendón, E., et al., 2014. Iber: herramienta de simulación numérica del flujo en ríos. Rev. Int. Métodos Numér. Para Cálc. Diseño Ing. 30 (1), 1–10. https://doi.org/10.1016/j.rimni.2012.07.004.

Broich, K., Pflugbeil, T., Disse, M., Nguyen, H., 2019. Using TELEMAC-2D for hydrodynamic modeling of rainfall-runoff. In: Presented at the Telemac User Conference 2019 (TUC2019). Zenodo. https://doi.org/10.5281/ZENODO.3611524.

Brotzge, J.A., Wang, J., Thorncroft, C.D., Joseph, E., Bain, N., Bassill, N., et al., 2020. A technical overview of the New York State Mesonet standard network. J. Atmos. Ocean. Technol. 37 (10), 1827–1845. https://doi.org/10.1175/JTECH-D-19-0220.1.

Carr, A.B., Trigg, M.A., Haile, A.T., Bernhofen, M.V., Alemu, A.N., Bekele, T.W., Walsh, C.L., 2024. Using global datasets to estimate flood exposure at the city scale: an evaluation in Addis Ababa. Front. Environ. Sci. 12, 1330295. https://doi.org/10.3389/fenvs.2024.1330295.

Cea, L., Sañudo, E., Montalvo, C., Farfán, J., Puertas, J., Tamagnone, P., 2025. Recent advances and future challenges in urban pluvial flood modelling. Urban Water J. 22 (2), 149–173. https://doi.org/10.1080/1573062X.2024.2446528.

Chaudhry, M.H., 2008. Open-Channel Flow. Springer US, Boston, MA. https://doi.org/10.1007/978-0-387-68648-6.

Chegini, T., Li, H.-Y., 2022. An algorithm for deriving the topology of belowground urban stormwater networks. Hydrol. Earth Syst. Sci. 26 (16), 4279–4300. https://doi.org/10.5194/hess-26-4279-2022.

Chen, Z., Huang, G., 2024. Numerical simulation study on the effect of underground drainage pipe network in typical urban flood. J. Hydrol. 638, 131481. https://doi.org/10.1016/j.jhydrol.2024.131481.

Chinchella, E., Cauteruccio, A., Lanza, L.G., 2025. Modelling the role of permeable pavements in mitigating pluvial flooding in Genoa, Italy. J. Hydrol.: Reg. Stud. 60, 102596. https://doi.org/10.1016/j.ejrh.2025.102596.

City of New York, 2025. NYC Open Data [Data Set]. https://opendata.cityofnewyork.us.

CRED, & UNDRR, 2020. The Human Cost of Disasters: an Overview of the Last 20 Years (2000-2019). Retrieved from. https://www.undrr.org/publication/human-cost-disasters-overview-last-20-years-2000-2019.

De Almeida, G.A.M., Bates, P., Freer, J.E., Souvignet, M., 2012. Improving the stability of a simple formulation of the shallow water equations for 2-D flood modeling. Water Resour. Res. 48 (5), 2011WR011570. https://doi.org/10.1029/2011WR011570.

DEFRA, 2006. *Flood Risk Assessment Guidance For New Development* (No. FD2320/TR2). UK Department for Environment, Food & Rural Affairs. Retrieved from. https://assets.publishing.service.gov.uk/media/602d040fd3bf7f721a23a993/Flood_risk_assessment_guidance_for_new_development_-_phase_2_technical_report_Full_Documentation_and_Tools.pdf.

DEP (Department of Environmental Protection), 2017. NYCDEP Citywide Catch Basins [Data set]. Retrieve from https://data.cityofnewyork.us/Environment/NYCDEP-Citywide-Catch-Basins/2w2g-fk3i/about_data.

DPR (Department of Parks and Recreation), 2017. Street Tree Census - Tree data (2015) [Data Set]. Retrieved from https://data.cityofnewyork.us/Environment/2015-Street-Tree-Census-Tree-Data/uvpi-gqnh/about_data.

Drews, M., Steinhausen, M., Larsen, M.A.D., Dømgaard, M.L., Huszti, L., Rácz, T., et al., 2023. The utility of using volunteered geographic information (VGI) for evaluating pluvial flood models. Sci. Total Environ. 894, 164962. https://doi.org/10.1016/j.scitotenv.2023.164962.

Environment Agency, H. H., 2019. What is the Risk of Flooding from Surface Water Map? Retrieved from. https://assets.publishing.service.gov.uk/government/uploads/system/uploads/attachment_data/file/842485/What-is-the-Risk-of-Flooding-from-Surface-Water-Map.pdf.

FEMA, 2018. Guidance For Flood Risk Analysis and Mapping. Flood Depth and Analysis Grids. Federal Emergency Management Agency. Retrieved from. https://www.fema.gov/sites/default/files/2020-02/Flood_Depth_and_Analysis_Grids_Guidance_Feb_2018.pdf.

FEMA, 2023a. Flood Risk Analysis and Mapping. Federal Emergency Management Agency.

FEMA, 2023b. *Effects of Hurricane Ida* (Mitigation Assessment Team Compendium Report). Federal Emergency Management Agency, New York City. Retrieved from. https://www.fema.gov/sites/default/files/documents/fema_p-2333-ida-compendium.pdf.

FEMA, 2025. Guidelines and Standards for Flood Risk Analysis and Mapping Activities Under the Risk MAP Program. Retrieved from. https://www.fema.gov/flood-maps/guidance-reports/guidelines-standards.

Feng, B., Zhang, Y., Bourke, R., 2021. Urbanization impacts on flood risks based on urban growth data and coupled flood models. Nat. Hazards 106 (1), 613–627. https://doi.org/10.1007/s11069-020-04480-0.

Fraga, I., Cea, L., Puertas, J., 2017. Validation of a 1D-2D dual drainage model under unsteady part-full and surcharged sewer conditions. Urban Water J. 14 (1), 74–84. https://doi.org/10.1080/1573062X.2015.1057180.

Gallegos, H.A., Schubert, J.E., Sanders, B.F., 2009. Two-dimensional, high-resolution modeling of urban dam-break flooding: a case study of Baldwin Hills, California. Adv. Water Resour. 32 (8), 1323–1335. https://doi.org/10.1016/j.advwatres.2009.05.008.

Gold, A., Anarde, K., Grimley, L., Neve, R., Srebnik, E.R., Thelen, T., et al., 2023. Data from the drain: a sensor framework that captures multiple drivers of chronic coastal floods. Water Resour. Res. 59 (4), e2022WR032392. https://doi.org/10.1029/2022WR032392.

Gradeci, K., Labonnote, N., Sivertsen, E., Time, B., 2019. The use of insurance data in the analysis of surface water flood events – A systematic review. J. Hydrol. 568, 194–206. https://doi.org/10.1016/j.jhydrol.2018.10.060.

Green, W., Ampt, G.A., 1911. Studies on soil physics. J. Agric. Sci. 4 (1), 1–24. https://doi.org/10.1017/S0021859600001441.

Guan, M., Guo, K., Yan, H., Wright, N., 2023. Bottom-up multilevel flood hazard mapping by integrated inundation modelling in data scarce cities. J. Hydrol. 617, 129114. https://doi.org/10.1016/j.jhydrol.2023.129114.

Guo, K., Guan, M., Yan, H., 2023. Utilising social media data to evaluate urban flood impact in data scarce cities. Int. J. Disaster Risk Reduct. 93, 103780. https://doi.org/10.1016/j.ijdrr.2023.103780.

Hammond, M.J., Chen, A.S., Djordjević, S., Butler, D., Mark, O., 2013. Urban flood impact assessment: a state-of-the-art review. Urban Water J. 12 (1), 14–29. https://doi.org/10.1080/1573062X.2013.857421.

Hartke, S.H., Wright, D.B., Li, Z., Maggioni, V., Kirschbaum, D.B., Khan, S., 2022. Ensemble representation of satellite precipitation uncertainty using a nonstationary, anisotropic autocorrelation model. Water Resour. Res. 58 (8), e2021WR031650. https://doi.org/10.1029/2021WR031650.

Hervouet, J., 2007. *Hydrodynamics of Free Surface Flows: Modelling with the Finite Element Method* (1st ed.). Wiley. https://doi.org/10.1002/9780470319628.

Hirabayashi, S., 2013. I-Tree Eco Precipitation Interception Model Descriptions.

Hjelmstad, A., Shrestha, A., Garcia, M., Mascaro, G., 2021. Propagation of radar rainfall uncertainties into urban pluvial flood modeling during the North American monsoon. Hydrol. Sci. J. 66 (15), 2232–2248. https://doi.org/10.1080/02626667.2021.1980216.

Hobley, D.E.J., Adams, J.M., Nudurupati, S.S., Hutton, E.W.H., Gasparini, N.M., Istanbulluoglu, E., Tucker, G.E., 2017. Creative computing with Landlab: an open-source toolkit for building, coupling, and exploring two-dimensional numerical models of Earth-surface dynamics. Earth Surf. Dyn. 5 (1), 21–46. https://doi.org/10.5194/esurf-5-21-2017.

Hollis, G.E., 1975. The effect of urbanization on floods of different recurrence interval. Water Resour. Res. 11 (3), 431–435. https://doi.org/10.1029/WR011i003p00431.

Hunter, N.M., Horritt, M.S., Bates, P.D., Wilson, M.D., Werner, M.G.F., 2005. An adaptive time step solution for raster-based storage cell modelling of floodplain inundation. Adv. Water Resour. 28 (9), 975–991. https://doi.org/10.1016/j.advwatres.2005.03.007.

Hydrologic Engineering Center, 2021. HEC-RAS 2D Modeling user's Manual. U.S. Army Corps of Engineers.

Hydrologic Engineering Center, 2024. HEC-RAS 2D Version 6.6. September. U.S. Army Corps of Engineers.

Ivanov, V.Y., Xu, D., Dwelle, M.C., Sargsyan, K., Wright, D.B., Katopodes, N., et al., 2021. Breaking down the computational barriers to real-time urban flood forecasting. Geophys. Res. Lett. 48 (20), e2021GL093585. https://doi.org/10.1029/2021GL093585.

Jacobson, C.R., 2011. Identification and quantification of the hydrological impacts of imperviousness in urban catchments: a review. J. Env. Manage 92 (6), 1438–1448. https://doi.org/10.1016/j.jenvman.2011.01.018.

Kasaei, S., Orton, P.M., Ralston, D.K., Warner, J.C., 2025. Pluvial and potential compound flooding in a coupled coastal modeling framework: new York City during post-tropical Cyclone Ida (2021). Hydrol. Earth Syst. Sci. 29 (8), 2043–2058. https://doi.org/10.5194/hess-29-2043-2025.

Li, D., Hou, J., Xia, J., Tong, Y., Yang, D., Zhang, D., Gao, X., 2020. An efficient method for approximately simulating drainage capability for urban flood. Front. Earth Sci. 8, 159. https://doi.org/10.3389/feart.2020.00159.

LISFLOOD-FP Developers, 2022. LISFLOOD-FP 8.1 Hydrodynamic Model (Version 8.1). September 23. Zenodo. https://doi.org/10.5281/ZENODO.6912932.

Mascaro, G., 2025. Codes and Data For Urban Flood Simulations [Data Set]. HydroShare. Retrieved from. https://www.hydroshare.org/resource/6cf42a4b61404099a3732147689f54b6.

Mascaro, G., Papalexiou, S.M., Wright, D.B., 2023. Advancing characterization and modeling of space-time correlation structure and marginal distribution of short-duration precipitation. Adv. Water Resour. 177, 104451. https://doi.org/10.1016/j.advwatres.2023.104451.

Metz, M., Mitasova, H., Harmon, R.S., 2011. Efficient extraction of drainage networks from massive, radar-based elevation models with least cost path search. Hydrol. Earth Syst. Sci. 15 (2), 667–678. https://doi.org/10.5194/hess-15-667-2011.

Mignot, E., Li, X., Dewals, B., 2019. Experimental modelling of urban flooding: a review. J. Hydrol. 568, 334–342. https://doi.org/10.1016/j.jhydrol.2018.11.001.

Moftakhari, H.R., AghaKouchak, A., Sanders, B.F., Allaire, M., Matthew, R.A., 2018. What is nuisance flooding? Defining and monitoring an emerging challenge. Water Resour. Res. 54 (7), 4218–4227. https://doi.org/10.1029/2018WR022828.

Molinari, D., De Bruijn, K.M., Castillo-Rodríguez, J.T., Aronica, G.T., Bouwer, L.M., 2019. Validation of flood risk models: current practice and possible improvements. Int. J. Disaster Risk Reduct. 33, 441–448. https://doi.org/10.1016/j.ijdrr.2018.10.022.

Montalvo, C., Reyes-Silva, J.D., Sañudo, E., Cea, L., Puertas, J., 2024. Urban pluvial flood modelling in the absence of sewer drainage network data: a physics-based approach. J. Hydrol. 634, 131043. https://doi.org/10.1016/j.jhydrol.2024.131043.

Mustafa, A., Szydłowski, M., 2021. Application of different building representation techniques in HEC-RAS 2-D for urban flood modeling using the Toce River experimental case. PeerJ 9, e11667. https://doi.org/10.7717/peerj.11667.

Mydlarz, C., Sai Venkat Challagonda, P., Steers, B., Rucker, J., Brain, T., Branco, B., et al., 2024. FloodNet: low-cost ultrasonic sensors for real-time measurement of hyperlocal, street-level floods in New York City. Water Resour. Res. 60 (5), e2023WR036806. https://doi.org/10.1029/2023WR036806.

National Academies of Sciences, Engineering, and Medicine, 2019. Framing the Challenge of Urban Flooding in the United States. National Academies Press, Washington, D.C., 25381. https://doi.org/10.17226/25381

NCEI, 2025. U.S. Billion-Dollar Weather and Climate Disasters. NOAA National Centers for Environmental Information. Retrieved from. https://www.ncei.noaa.gov/access/billions/.

NYC 311. (n.d.). Catch basin complaint. Retrieved from https://portal.311.nyc.gov/article/?kanumber=KA-01084.

NYC DEP, 2021. New York City Department of Environmental Protection (DEP) official Facebook page. https://www.facebook.com/photo.php?fbid=10159937894594589&id=339406479588&set=a.442629339588.

NYC Mayor's Office of Resiliency, 2021. New York City Stormwater Resiliency Plan. Retrieved from. https://climate.cityofnewyork.us/reports/nyc-stormwater-resiliency-plan/.

Oberauer, M., Lehmann, B., 2023. Modifying 2D surface models in urban flood analysis. J. Hydrol. 625, 130063. https://doi.org/10.1016/j.jhydrol.2023.130063.

Oberauer, M., Lehmann, B., 2024. Enhanced 2D-models as alternative to dual-drainage systems for urban flood simulation. J. Hydrol. 645, 132198. https://doi.org/10.1016/j.jhydrol.2024.132198.

Ochoa-Rodriguez, S., Wang, L.-P., Gires, A., Pina, R.D., Reinoso-Rondinel, R., Bruni, G., et al., 2015. Impact of spatial and temporal resolution of rainfall inputs on urban hydrodynamic modelling outputs: a multi-catchment investigation. J. Hydrol. 531, 389–407. https://doi.org/10.1016/j.jhydrol.2015.05.035.

OTI (Office of Technology and Innovation), 2017. Land Cover raster Data (2017) [Data Set]. Retrieved from https://data.cityofnewyork.us/Environment/Land-Cover-Raster-Data-2017-6in-Resolution/he6d-2qns/about_data.

OTI (Office of Technology and Innovation), 2016. Building Footprints [Data set]. Retrieved from https://data.cityofnewyork.us/City-Government/Building-Footprints-Map-/jh45-qr5r.

Partners, O.C.M., 2017. 2017 NYC Topobathy Lidar Hydroenforced DEM: New York City [Data set]. NOAA National Centers for Environmental Information. https://www.fisheries.noaa.gov/inport/item/64734.

Palla, A., Colli, M., Candela, A., Aronica, G.T., Lanza, L.G., 2018. Pluvial flooding in urban areas: the role of surface drainage efficiency. J. Flood Risk Manag. 11 (S2). https://doi.org/10.1111/jfr3.12246.

Papalexiou, S.M., Serinaldi, F., Porcu, E., 2021. Advancing space-time simulation of random fields: from storms to cyclones and beyond. Water Resour. Res. 57 (8), e2020WR029466. https://doi.org/10.1029/2020WR029466.

Pasch, R.J., Berg, R., Hagen, A.B., 2022. *Hurricane Henri* (Tropical Cyclone Report). National Hurricane Center. Retrieved from. https://www.nhc.noaa.gov/data/tcr/AL082021_Henri.pdf.

Peleg, N., Fatichi, S., Paschalis, A., Molnar, P., Burlando, P., 2017. An advanced stochastic weather generator for simulating 2-D high-resolution climate variables. J. Adv. Model. Earth Syst. 9 (3), 1595–1627. https://doi.org/10.1002/2016MS000854.

Peleg, N., Ban, N., Gibson, M.J., Chen, A.S., Paschalis, A., Burlando, P., Leitão, J.P., 2022. Mapping storm spatial profiles for flood impact assessments. Adv. Water Resour. 166, 104258. https://doi.org/10.1016/j.advwatres.2022.104258.

Perica, S., Pavlovic, S., St Laurent, M., Trypaluk, C., Unruh, D., Martin, D., Wilhite, O., 2015. NOAA Atlas 14 Precipitation-Frequency Atlas of the United States Volume 10 Version 3.0: Northeastern States Connecticut, Maine, Massachusetts, New Hampshire, New York, Rhode Island, Vermont. NOAA, National Weather Service, Texas.

QGIS Development Team, 2019. QGIS Geographic Information System. QGIS Association. Retrieved from. https://www.qgis.org.

Rong, Y., Bates, P., Neal, J., Archer, L., Hatchard, S., Kendon, E., 2024. Impact of soil moisture dynamics and precipitation pattern on UK urban pluvial flood hazards under climate change. Earth's Fut. 12 (5), e2023EF004073. https://doi.org/10.1029/2023EF004073.

Rosenzweig, B.R., McPhillips, L., Chang, H., Cheng, C., Welty, C., Matsler, M., et al., 2018. Pluvial flood risk and opportunities for resilience. WIREs Water 5 (6), e1302. https://doi.org/10.1002/wat2.1302.

Rosenzweig, B.R., Herreros Cantis, P., Kim, Y., Cohn, A., Grove, K., Brock, J., et al., 2021. The value of urban flood modeling. Earth's Fut. 9 (1), e2020EF001739. https://doi.org/10.1029/2020EF001739.

Sampson, C.C., Bates, P.D., Neal, J.C., Horritt, M.S., 2013. An automated routing methodology to enable direct rainfall in high resolution shallow water models. Hydrol. Process. 27 (3), 467–476. https://doi.org/10.1002/hyp.9515.

Sanders, B.F., Schubert, J.E., 2019. PRIMo: parallel raster inundation model. Adv. Water Resour. 126, 79–95. https://doi.org/10.1016/j.advwatres.2019.02.007.

Sañudo, Cea, L., Puertas, J., 2020. Modelling pluvial flooding in urban areas coupling the models Iber and SWMM. Water 12 (9), 2647. https://doi.org/10.3390/w12092647.

Sañudo, E., García-Feal, O., Hagen, L., Cea, L., Puertas, J., Montalvo, C., et al., 2025. IberSWMM+: a high-performance computing solver for 2D-1D pluvial flood modelling in urban environments. J. Hydrol. 651, 132603. https://doi.org/10.1016/j.jhydrol.2024.132603.

Sanz-Ramos, M., Sañudo, E., López-Gómez, D., García-Feal, O., Bladé, E., Cea, L., 2025. Evolución de la modelización numérica bidimensional del flujo en lámina libre a través del software Iber. Ing. Agua 29 (2), 114–131. https://doi.org/10.4995/ia.2025.23259.

Schmitt, T.G., Scheid, C., 2020. Evaluation and communication of pluvial flood risks in urban areas. WIREs Water 7 (1), e1401. https://doi.org/10.1002/wat2.1401.

Schubert, J.E., Sanders, B.F., 2012. Building treatments for urban flood inundation models and implications for predictive skill and modeling efficiency. Adv. Water Resour. 41, 49–64. https://doi.org/10.1016/j.advwatres.2012.02.012.

Schubert, J.E., Mach, K.J., Sanders, B.F., 2024. National-scale flood hazard data unfit for urban risk management. Earth's Fut. 12 (7), e2024EF004549. https://doi.org/10.1029/2024EF004549.

Sharifian, M.K., Kesserwani, G., Chowdhury, A.A., Neal, J., Bates, P., 2023. LISFLOOD-FP 8.1: new GPU-accelerated solvers for faster fluvial/pluvial flood simulations. Geosci. Model Dev. 16 (9), 2391–2413. https://doi.org/10.5194/gmd-16-2391-2023.

Shaw, J., Kesserwani, G., Neal, J., Bates, P., Sharifian, M.K., 2021. LISFLOOD-FP 8.0: the new discontinuous Galerkin shallow-water solver for multi-core CPUs and GPUs. Geosci. Model Dev. 14 (6), 3577–3602. https://doi.org/10.5194/gmd-14-3577-2021.

Singh, A., Dawson, D., Trigg, M.A., Wright, N., Seymour, C., Ferriday, L., 2023. Drainage representation in flood models: application and analysis of capacity assessment framework. J. Hydrol. 622, 129718. https://doi.org/10.1016/j.jhydrol.2023.129718.

Soil Survey Staff, Natural Resources Conservation Service, & United States Department of Agriculture, 2025. Official Soil Series Descriptions [Data set]. Retrieved from. https://www.nrcs.usda.gov/resources/data-and-reports/official-soil-series-descriptions-osd.

Son, Y., Di Lorenzo, E., Park, K., Wipperfurth, S., Luo, J., 2023. Data assimilation of hyper-local water level sensors for real-time monitoring of coastal inundation. Coast. Eng. 186, 104398. https://doi.org/10.1016/j.coastaleng.2023.104398.

Surendran, S., Geoff, G., Wade, S., Udale-Clarke, H., 2008. *Supplementary note on flood hazard ratings and thresholds for development planning and control purpose* (No. FD2320/TR2). Retrieved from. https://assets.publishing.service.gov.uk/media/602d04a98fa8f5037d371a08/FLOOD_HAZARD_RATINGS_AND_THRESHOLDS_explanatory_note.pdf.

Underwood, B.S., Mascaro, G., Chester, M.V., Fraser, A., Lopez-Cantu, T., Samaras, C., 2020. Past and present design practices and uncertainty in climate projections are challenges for designing infrastructure to future conditions. J. Infrastruct. Syst. 26 (3), 04020026. https://doi.org/10.1061/(ASCE)IS.1943-555X.0000567.

Van Der Sande, C.J., De Jong, S.M., De Roo, A.P.J., 2003. A segmentation and classification approach of IKONOS-2 imagery for land cover mapping to assist flood risk and flood damage assessment. Int. J. Appl. Earth Obs. Geoinf. 4 (3), 217–229. https://doi.org/10.1016/S0303-2434(03)00003-5.

Wang, Y., Chen, A.S., Fu, G., Djordjević, S., Zhang, C., Savić, D.A., 2018. An integrated framework for high-resolution urban flood modelling considering multiple information sources and urban features. Environ. Model. Softw. 107, 85–95. https://doi.org/10.1016/j.envsoft.2018.06.010.

WPC, 2023. Weather Prediction Center Archive of the National Forecast Chart. September 29. Retrieved December 19, 2024, from. https://www.wpc.ncep.noaa.gov/noaa/noaa_archive.php.

Wu, X., Wang, Z., Guo, S., Lai, C., Chen, X., 2018. A simplified approach for flood modeling in urban environments. Hydrol. Res. 49 (6), 1804–1816. https://doi.org/10.2166/nh.2018.149.

Xia, J., Dong, B., Zhou, M., Ahmadian, R., Falconer, R.A., Li, Q., Zhang, X., 2022. A unified formula for discharge capacity of street inlets for urban flood management. J. Hydrol. 609, 127667. https://doi.org/10.1016/j.jhydrol.2022.127667.

Xiang, M., Zhang, S., Wu, C., Tang, C., 2024. A two-dimensional hydrodynamic urban flood model based on equivalent drainage of manholes. J. Hydroinform. 26 (2), 519–533. https://doi.org/10.2166/hydro.2024.240.

Xing, Y., Shao, D., Liang, Q., Chen, H., Ma, X., Ullah, I., 2022. Investigation of the drainage loss effects with a street view based drainage calculation method in hydrodynamic modelling of pluvial floods in urbanized area. J. Hydrol. 605, 127365. https://doi.org/10.1016/j.jhydrol.2021.127365.

Yang, W., Zheng, C., Jiang, X., Wang, H., Lian, J., Hu, D., Zheng, A., 2023. Study on urban flood simulation based on a novel model of SWTM coupling D8 flow direction and backflow effect. J. Hydrol. 621, 129608. https://doi.org/10.1016/j.jhydrol.2023.129608.

Yu, D., Coulthard, T.J., 2015. Evaluating the importance of catchment hydrological parameters for urban surface water flood modelling using a simple hydro-inundation model. J. Hydrol. 524, 385–400. https://doi.org/10.1016/j.jhydrol.2015.02.040.

Zhang, J., & Gourley, J. (2018). Multi-Radar Multi-Sensor precipitation reanalysis (Version 1.0) (Version 1.0) [Data set]. https://doi.org/10.25638/EDC.PRECIP.0001.

Zhou, Z., Smith, J.A., Baeck, M.L., Wright, D.B., Smith, B.K., Liu, S., 2021. The impact of the spatiotemporal structure of rainfall on flood frequency over a small urban watershed: an approach coupling stochastic storm transposition and hydrologic modeling. Hydrol. Earth Syst. Sci. 25 (9), 4701–4717. https://doi.org/10.5194/hess-25-4701-2021.